(Received 23 July 2025, Accepted 15 October 2025, Scheduled 31 October 2025)

Research on Multi-Vehicle Beam Tracking Algorithm Based on Aerial Reconfigurable Intelligent Surface Assistance

Chenwei Feng*, Zhenzhen Lin, Yawei Sun, Yangbin Huang, and Yinhua Wu

School of Opto-Electronic and Communication Engineering, Xiamen University of Technology, Xiamen 361000, China

ABSTRACT: With the growth of demand for high-rate and high-quality wireless communication services, Unmanned Aerial Vehicle (UAV) communication technology has received a lot of attention. By deploying Reconfigurable Intelligent Surface (RIS) on the UAV, more users can be reached while effectively expanding the signal coverage. The rotational nature of the UAV also provides new degrees of freedom in the design of RIS-assisted millimeter-wave Multiple Input Multiple Output (MIMO) systems. In this paper, using the advantages of UAV and RIS technologies, Aerial Reconfigurable Intelligent Surface (ARIS) is introduced to assist the communication, and the millimeter-wave Vehicle to Infrastructure (V2I) communication scenario based on the ARIS-assisted multi-vehicle beam tracking problem. First, Zero Forcing (ZF) beamforming is employed at the base station to eliminate inter-vehicle interference. On this basis, the vehicle-side beam combining matrix, RIS-side reflection beamforming matrix, along with the rotation angle of the ARIS, are jointly designed to maximize the number of vehicles and data rates, thereby providing high-quality communication for beam tracking studies. Secondly, an ARIS-assisted multi-vehicle beam tracking model is derived in a MIMO-based 3D communication scenario. Finally, an Extended Kalman Filter (EKF) algorithm based on the angular deviation correction mechanism is proposed to realize the beam tracking of multiple vehicles. Simulation results show that the proposed EKF algorithm can effectively reduce the beam tracking error in multi-vehicle communication scenarios with robust beam tracking capability under the joint design based on beam merging matrix, beamforming matrix, and ARIS rotation angle.

1. INTRODUCTION

In wireless communication systems, MIMO technology not only realizes high-rate information transmission, but also provides users with high-gain directional beams through beamforming, which is regarded as a key technology to support the development of Internet of Vehicles (IoV) [1–4]. However, this directionality makes it necessary to switch beams frequently to achieve beam alignment in dynamic scenes, which incurs significant system overhead. Therefore, for IoV scenarios, it is necessary to use a low-complexity beam tracking technique to track the beam direction and achieve beam alignment at the receiver and transmitter ends to ensure a stable connection of the communication link. In addition, millimeter waves are susceptible to occlusions resulting in failure to communicate properly, which in turn degrades the performance of beam tracking. RIS, as one of the potential key technologies for 6G, can effectively solve the problem of millimeter-wave link obstruction by constructing an intelligent and controllable wireless transmission environment [5–8].

In IoV systems, when the Line of Sight (LoS) path of the BS-UE is disconnected by obstacles, the Virtual Line of Sight (VLoS) transmission path constructed by RIS can be utilized to achieve reliable communication in the occluded area [9, 10]. With the assistance of RIS, it effectively reduces the coverage blind spot of IoV in high-density urban clusters, improves network connectivity, and enables stable and reliable V2I communication. Meanwhile, in the process of using RIS to assist in the optimization of wireless communication systems, the key challenge is how to cooperatively optimize beamforming at both the base station side and RIS side in order to achieve system performance goals. RIS generally consists of a series of low-cost electromagnetic reflective units that are programmed to adjust the bias voltage of each unit to control the phase of the electromagnetic waves radiated by that unit, introducing additional beamforming to the communication system [11]. Optimizing only the beamforming at the base station end and ignoring the phase shift configuration design of the RIS will result in the reflected beam not being accurately aligned to the user, thus limiting the potential gain in system performance. Only through the joint beamforming design of the base station side and RIS side can precise control of the signal transmission direction be realized, so as to establish high-quality communication between the transceiver side and give full play to the technical advantages of RIS [12]. From the perspective of mathematical analysis, beamforming design is usually constructed as an optimization problem, where constraints such as minimum Signal-to-Noise Ratio (SNR) constraint, maximum power constraint of the base station, and the modulation capability of the antenna are satisfied, and the performance of the system is improved by taking the maximization of spectral and energy efficiencies, the maximization of the sum-rate of multiusers, the maximization of the minimum SNR of multiusers, etc. as the optimization objectives to improve the system performance. In RIS-assisted wireless communication systems, the optimization model for beamforming is generally more complex, and its specific form presents differences depending on

* Corresponding author: Chenwei Feng (cwfeng@xmut.edu.cn).

the application scenario. This variability depends mainly on the antenna configuration scheme at the transceiver end (single antenna or multi-antenna array), the number of RISs deployed in the system (single RIS or multiple RISs), and the distribution of users (single user or multiple users). The introduction of RIS provides a new development path for future mobile communications, but RIS also has its limitations. Ground-based RISs are usually placed on the surface of buildings, where the location is fixed and difficult to optimize, and can only provide a 180° reflective span, limiting coverage capabilities. In addition, in complex environments such as cities, the signal from the transmitter to the receiver may need to be reflected by multiple RISs in order to bypass the intervening obstacles, which, although effective in overcoming the occlusion problem, leads to severe path loss [13]. UAV has received extensive attention and research in wireless communication networks due to its significant advantages such as low cost, high mobility, and flexible deployment on demand [14–17]. Carrying RIS through the UAV to aid communication with an ARIS allows for 360° omnidirectional reflections and the ability to establish higher probability LoS links for better channel conditions. In addition, ARIS can further enhance the performance of the communication network by flexibly adjusting its position and using its high mobility to enhance signal coverage and fill in blind spots. ARIS is also more flexible in terms of layout compared to ground-based RIS [18] and provides a new paradigm for land and air-ground communications through the new three-dimensional wireless networks it enables. In addition, ARIS effectively overcomes the shortcomings of a single UAV. Specifically, low-cost UAVs are limited by on-board battery capacity and communication bandwidth resources, making it difficult to meet the functional requirements of small flying base stations. ARIS can significantly reduce the energy consumption of UAVs by optimizing the propagation path of wireless signals. In contrast to the need to frequently adjust the UAV position to adapt to the user's mobility, ARIS can dynamically adjust the phase shift of the RIS to establish a new LoS link, thus avoiding the energy loss and delay problems of UAVs due to frequent movement. In addition, the RIS mounted on a UAV has a rotational character, which provides a new degree of freedom for the optimization of RIS-assisted millimeter-wave MIMO communication systems [19]. In summary, the research of beam tracking technology in millimeter-wave IoV scenarios can be assisted by combining the advantages of UAV and RIS with ARIS.

In the study of RIS-assisted wireless communication based on RIS, [20] studied the channel tracking problem of RIS-assisted millimeter-wave Multiple-Input Single-Output (MISO) system, which employs a traceless Kalman filtering algorithm to track the channel parameters. In order to minimize the mean square error of the tracking parameters, the beamforming vectors at the base station end and the reflection vectors at the RIS are iteratively designed, and the resulting sub-problems are solved by the semipositive definite relaxation method and Gaussian stochastic method. Ref. [21] investigates the channel estimation problem in RIS-assisted multiuser networks taking into account user mobility. Using the KF tracking cascade channel, expressions for the state and measurement covariance matrices for the case of Rice fading and pilot frequency contamination are derived, and the discrete Fourier transform matrix is used as the phase shift matrix. Ref. [22] addresses the RIS-assisted millimeter-wave MIMO downlink system with the optimization objective of maximizing multiple users and rates by co-optimizing the passive beamforming, power allocation, precoding matrices, and merging matrices for RIS by utilizing flow optimization techniques. Ref. [23] derives a per-user resolved downlink error rate (SER) as a function of phase shift and beamforming vectors for RIS-assisted multiuser scenarios and proposes an average SER minimization problem. In optimizing the active and passive beamforming variables in an RIS-aided communication system, differential evolution algorithm is used to address the non-convexity of the considered SER optimization problem, and local search is introduced. Ref. [24], for a multi-RIS-aided multi-vehicle MIMO V2I network, an alternating optimization-based method is proposed to jointly optimize the transmitter beamforming and RIS phase shifts. The max-min quality of service is achieved in the form of weighted Signal to Interference plus Noise Ratio (SINR).

The introduction of UAV and RIS to assist the communication in wireless communication systems has been widely studied and applied. Ref. [25] studies the problem of secure communication in ARIS-based multi-user networks. The problem is modeled as a secrecy rate maximization problem with channel uncertainty constraints. Since it is a non-convex problem, it is decomposed into beamforming, phase-shifting, and UAV trajectory subproblems. Ref. [26] constructes a weighted and rate maximization problem for ARIS-assisted multiuser MISO communication networks by jointly optimizing the transmit beamforming and ARIS phase shift at the base station end and proposes a solution based on the block coordinate descent method and Lagrangian dyadic transform. Ref. [27] studies a multi-user localization scheme in RIS-assisted UAV millimeter-wave wireless networks and proposes an alternating algorithm that minimizes the maximum position error bound among all users by iteratively optimizing the UAV trajectory, user scheduling, UAV beamforming, and RIS phase shifting until convergence. Ref. [28] uses ZF precoding in the beamforming design at the base station end for multi-ARIS scenarios and developes an iterative algorithm based on first-order approximation, block coordinate descent, and alternating optimization aiming at maximizing the network throughput by optimizing the power control coefficients at the base station end and phase shifts for multiple RISs.

Most of the existing studies on beamforming for RIS-assisted wireless communications are for single RIS-assisted single-user MISO or MIMO systems. The few beamforming designs for single RIS-assisted multiuser MIMO systems are also mainly based on iterative optimization algorithms, which usually have high time complexity, and at the same time need to pay attention to the convergence efficiency as well as avoiding falling into local optimums in the iterative solving process. This is for high-speed mobile scenarios, where the resulting time overhead increases the difficulty of beam alignment during communication and affects the quality of communication. Current research on single RIS-assisted millimeter-wave MIMO multiuser beam tracking also focuses on static environments

and lacks research on IoV scenarios, which has certain application limitations.

Based on the above, this paper deploys reconfigurable smart metasurfaces on UAVs, proposing an ARIS-assisted multi-vehicle beam tracking solution to fully leverage their high maneuverability and rotational freedom. The main research content is as follows. ZF beamforming is introduced at the base station side. The vehicle-side beam combining matrix, RIS reflection matrix, and ARIS rotation angle are jointly optimized. The maximization of the system sum rate is thus achieved; an ARIS-assisted three-dimensional beam tracking model was established and derived; an extended Kalman filter algorithm incorporating an angular deviation correction mechanism was proposed, effectively enhancing the accuracy and robustness of beam tracking. This provides a feasible and efficient solution for millimeter-wave communication in highly dynamic IoV.

The main contributions of this paper are summarized as follows:

(1) At the base station, ZF beamforming technology is employed to effectively eliminate inter-vehicle interference in multi-vehicle communication scenarios. Concurrently, with system and rate maximization as optimization objectives, the vehicle-side beam combining matrix, RIS-side reflection beamforming matrix, and ARIS rotation angle are designed jointly.

(2) The Kronecker product structure based on RIS antenna arrays decomposes the RIS beamforming optimization problem into low-dimensional horizontal and vertical subproblems for solution, effectively reducing computational complexity and making it suitable for millimeter-wave V2I scenarios. The user-end beam combining matrix is solved using the Singular Value Decomposition (SVD) method.

(3) A beam tracking model for ARIS-assisted multi-vehicle communication scenarios with rotational characteristics has been derived.

(4) Finally, an EKF algorithm based on an angular deviation correction mechanism is proposed to achieve multi-vehicle beam tracking. Building upon the traditional EKF algorithm, this approach incorporates angular deviation threshold detection, effectively suppressing the error accumulation caused by linearization approximations inherent in the EKF algorithm.

The remainder of this paper is organized as follows. Section 2 details the system model described herein. Section 3 introduces ARIS-assisted multi-vehicle beam tracking. Section 4 presents simulation results and analysis. Finally, Section 5 summarizes the entire paper.

2. SYSTEM MODEL

2.1. Scenario Model

Considering a unidirectional two-lane IoV scenario covered by a single Road Side Unit (RSU), where a single RIS is retrofitted to a UAV, and an ARIS is deployed in the air to assist the communication between the RSU and the vehicle user, the studied scenario model is shown in Figure 1. Communicate with multiple vehicle users at the same time via the reflective path of the ARIS within the communication coverage of the RSU. Based on millimeter-wave MIMO, signal transmission and reception are carried out, that is, both RSU and vehicle users are equipped with multiple antennas. In the research scenario of this paper, only the communication between the RSU and the vehicle user through the VLoS path constructed by ARIS is considered, that is, there is no communicating LoS path between the vehicle user and the RSU. Unlike previous RIS-assisted wireless communication models, this paper considers the ability of the RIS to rotate around its axis on the UAV, which can be controlled by a mechanical rotation device integrated underneath the UAV. In the millimeter-wave V2I scenario, the performance impact on beam tracking is investigated by introducing additional degrees of freedom provided by ARIS rotation. When an RIS-equipped UAV moves continuously from one position to another, it consumes a lot of energy. However, if the UAV remains in the same position while rotating the RIS by means of a low-power motor, the same or even better performance can be achieved without continuous movement. With this RIS rotation, the energy consumed is negligible compared to the continuous trajectory optimization of the UAV.

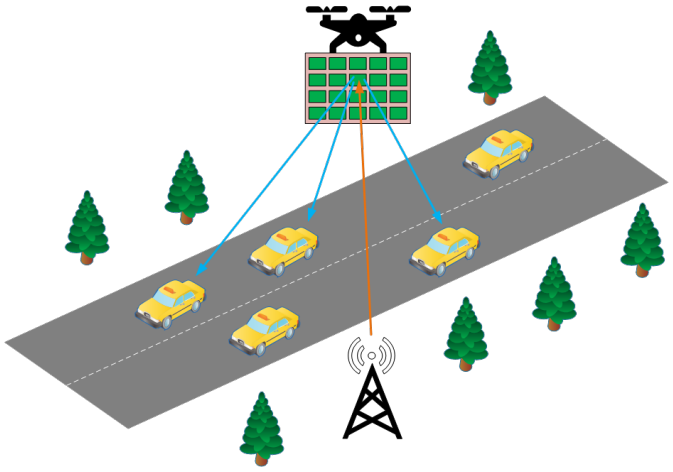

FIGURE 1. Scenario model.

2.2. Transmission Model

This paper focuses on the ARIS-assisted downlink V2I communication process. In millimeter-wave MIMO multi-vehicle systems, RSUs and ARIS jointly serve L vehicle users. Since the vehicle is in a highly mobile state, if the ARIS is moving in flight in either horizontal or vertical plane, both are in a dynamic state, which will inevitably increase the difficulty of aligning the RIS with the vehicle user's beam, and thus reduce the performance of beam tracking. In this paper, ARIS is considered to be fixedly deployed at a certain altitude from the ground, and the positions of ARIS and RSU are accurately acquired in advance. Taking the position of the fixed deployed RSU as the origin, the direction of vehicle driving is defined as the x-axis; the direction perpendicular to it as the y-axis; and

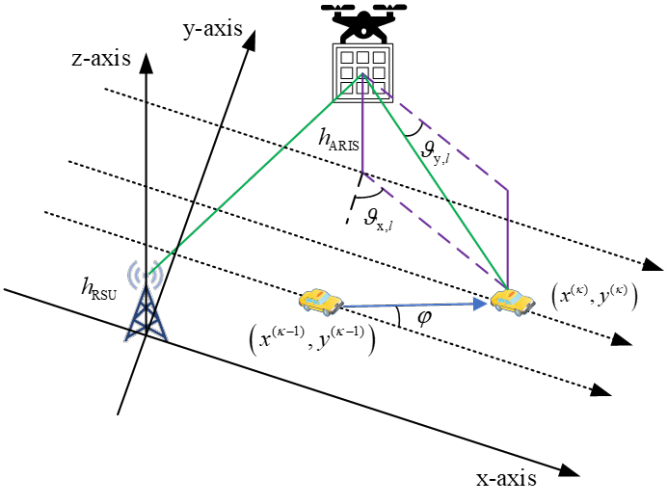

FIGURE 2. Study model.

the direction perpendicular to the road surface as the z-axis, in order to establish the three-dimensional spatial coordinate system. Taking a certain vehicle in the scenario as an example, the specific research model is shown in Figure 2. ARIS is deployed in the communication coverage area of the RSU to construct a VLoS path to reflect the communication beam. Assume that in the ideal case where there are no scattering points, there is only one LoS path between BS-ARIS and ARIS-UE, and there is no NLoS path due to scattering points. The number of antennas configured by the RSU is all N_{BS}, and the number of antennas configured by the vehicle users is N_{UE}, arranged in a Uniform Linear Array (ULA). ARIS consists of $N_{\text{ARIS}} = N_{\text{x}} \times N_{\text{y}}$ reflective units arranged in a Uniform Planar Array (UPA). Both antenna/unit spacings are set to $d = \lambda/2$, and λ is the signal wavelength.

Let $\mathbf{H}_{\text{BR}}$ and $\mathbf{H}_{\text{RU},l}$ denote the channels from the RSU to ARIS and from the ARIS to the lth vehicle, respectively, $\boldsymbol{\Theta} = \mathbf{diag}(\xi_1 e^{j\theta_1}, \xi_2 e^{j\theta_2}, \ldots, \xi_M e^{j\theta_M})$ be the reflection phase shift matrix at the ARIS, and the reflection coefficients and phase shifts of the mth EMU of the ARIS reflecting surface satisfy $\xi_m \in [0,1]$ and $\theta_m \in [0, 2\pi)$. The cascading channel model from the BS to the lth vehicle can be expressed as follows:

$$\mathbf{H}_{\text{BRU},l} = \mathbf{H}_{\text{RU},l} \boldsymbol{\Theta} \mathbf{H}_{\text{BR}} \tag{1}$$

Then, the received signal of vehicle l at discrete time κ can be expressed as:

$$r_l = \sqrt{\rho_l} \mathbf{w}_l^{\text{H}} \mathbf{H}_{\text{BRU},l} \mathbf{f}_l s_l + \sum_{j=1, j\neq l}^{L} \sqrt{\frac{P_j}{\sigma^2} \left(\frac{\lambda}{4\pi d_l}\right)^n} \mathbf{w}_l^{\text{H}} \mathbf{H}_{\text{BRU},l} \mathbf{f}_j s_j + n_l \tag{2}$$

where $\mathbf{w}_l$ is the beam merging vector of vehicle l; $\mathbf{f}_l$ is the beamforming vector of the transmitting end about vehicle l; s_l is the transmitting signal of vehicle l; $\sum_{j=1, j\neq l}^{L} \mathbf{w}_l^{\text{H}} \mathbf{H}_{\text{BRU},l} \mathbf{f}_j$ is the interference from other vehicles to vehicle l; n_l is the normalized noise, obeying a Gaussian distribution with mean 0 and variance 1; ρ_l is the average SNR of each antenna, which can be expressed as [29–31]:

$$\rho_l = \frac{P_l}{\sigma^2} \left(\frac{\lambda}{4\pi d_l}\right)^n \tag{3}$$

where the maximum transmit power at the transmitter is assumed to be P, and the transmitting power assigned to the lth vehicle is P_l. Then, it satisfies $\sum_{l=1}^{L} P_l \leq P$, and σ^2 is the noise power, n the path loss exponent, λ the wavelength, and d_l the distance of the VLoS path.

The cascading channel at discrete time κ is modeled based on the extended Saleh-Valenzuela channel model [32]. The channel $\mathbf{H}_{\text{BR}}$ from the BS to ARIS and the channel $\mathbf{H}_{\text{RU},l}^{(\kappa)}$ from the ARIS to the lth vehicle are denoted respectively:

$$\mathbf{H}_{\text{BR}} = \beta_{\text{BR}} \mathbf{a}_{\text{ARIS}} \left(\overline{\vartheta}_{\text{x}}, \overline{\vartheta}_{\text{y}}\right) \mathbf{a}_{\text{BS}}^{\text{H}} \left(\psi_{\text{BS}}\right) \tag{4}$$

$$\mathbf{H}_{\text{RU},l}^{(\kappa)} = \beta_{\text{RU},l}^{(\kappa)} \mathbf{a}_{\text{UE}} \left(\psi_{\text{UE},l}^{(\kappa)}\right) \mathbf{a}_{\text{ARIS}}^{\text{H}} \left(\vartheta_{\text{x},l}^{(\kappa)}, \vartheta_{\text{y},l}^{(\kappa)}\right) \tag{5}$$

where β_{BR} and $\beta_{\text{RU},l}^{(\kappa)}$ are the channel gain coefficients for the two segmented subchannels, BS-ARIS and ARIS-UE; $\mathbf{a}_{\text{ARIS}}$ is the UPA array response vector of ARIS; ψ_{BS} and $\psi_{\text{UE},l}^{(\kappa)}$ denote the beam pointing direction at BS and lth vehicle, respectively; $\overline{\vartheta}_{\text{x}}$ and $\overline{\vartheta}_{\text{y}}$ denote the azimuth and pitch angles of the beam in the ARIS incidence direction, respectively; $\vartheta_{\text{x},l}^{(\kappa)}$ and $\vartheta_{\text{y},l}^{(\kappa)}$ denote the azimuth and pitch angles of the beam in the ARIS reflection direction with respect to the first vehicle, respectively.

The gain coefficients β_{BR} and $\beta_{\text{RU},l}^{(\kappa)}$ of the two segmented subchannels can be expressed as functions of their corresponding link distances, respectively, as follows [33]:

$$\beta_{\text{BR}} = \tilde{\beta} d_{\text{BR}}^{-1} e^{j\frac{2\pi}{\lambda} d_{\text{BR}}} = \tilde{\beta} d_{\text{BR}}^{-1} e^{j\frac{2\pi f_c}{c} d_{\text{BR}}} \tag{6}$$

$$\beta_{\text{RU},l}^{(\kappa)} = \tilde{\beta} \left(d_{\text{RU},l}^{(\kappa)}\right)^{-1} e^{j\frac{2\pi}{\lambda} d_{\text{RU},l}^{(\kappa)}} = \tilde{\beta} \left(d_{\text{RU},l}^{(\kappa)}\right)^{-1} e^{j\frac{2\pi f_c}{c} d_{\text{RU},l}^{(\kappa)}} \tag{7}$$

where d_{BR} is the distance between the BS and ARIS; $d_{\text{RU},l}^{(\kappa)}$ is the distance between the ARIS and the lth vehicle; $\tilde{\beta}$ is the channel power gain at a reference distance of 1 m; β_{BR} is a fixed value; $\beta_{\text{RU},l}^{(\kappa)}$ is a time-varying value.

The ULA response vectors at the BS end and the lth UE end can be expressed as respectively:

$$\mathbf{a}_{\text{BS}} \left(\psi_{\text{BS}}\right) = \frac{1}{\sqrt{N_{\text{BS}}}} \left[1, e^{j\psi_{\text{BS}}}, \ldots, e^{j(N_{\text{BS}}-1)\psi_{\text{BS}}}\right]^{\text{T}} \tag{8}$$

$$\mathbf{a}_{\text{UE}} \left(\psi_{\text{UE},l}^{(\kappa)}\right) = \frac{1}{\sqrt{N_{\text{UE}}}} \left[1, e^{j\psi_{\text{UE},l}^{(\kappa)}}, \ldots, e^{j(N_{\text{UE}}-1)\psi_{\text{UE},l}^{(\kappa)}}\right]^{\text{T}} \tag{9}$$

The top view of the study model when ARIS is rotated is shown in Figure 3, when the azimuth angle is $\tilde{\vartheta}_{\text{x},l}^{(\kappa)}$. The UPA array response at ARIS in the incident and reflected directions can be expressed as respectively:

$$\mathbf{a}_{\text{ARIS}} \left(\overline{\vartheta}_{\text{x}}, \overline{\vartheta}_{\text{y}}, \alpha\right) = \mathbf{a}_{\text{x}} \left(\overline{\vartheta}_{\text{x}}, \alpha\right) \otimes \mathbf{a}_{\text{y}} \left(\overline{\vartheta}_{\text{y}}, \alpha\right) \tag{10}$$

$$\mathbf{a}_{\text{ARIS}} \left(\vartheta_{\text{x},l}^{(\kappa)}, \vartheta_{\text{y},l}^{(\kappa)}, \alpha\right) = \mathbf{a}_{\text{x},l} \left(\vartheta_{\text{x},l}^{(\kappa)}, \alpha\right) \otimes \mathbf{a}_{\text{y},l} \left(\vartheta_{\text{y},l}^{(\kappa)}, \alpha\right) \tag{11}$$

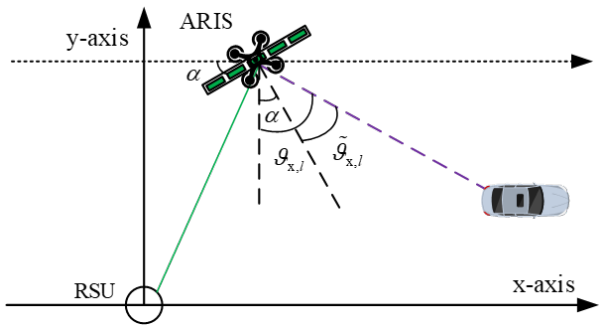

FIGURE 3. Top view of ARIS rotational model.

where α denotes the angle of rotation of ARIS, and $\otimes$ denotes the Kronecker product. The above two equations can be expressed in detail as:

$$\begin{aligned}\mathbf{a}_{\text{ARIS}}\left(\overline{\vartheta}_{\text{x}},\overline{\vartheta}_{\text{y}},\alpha\right)=&\frac{1}{\sqrt{N_{\text{ARIS}}}}\left[1,e^{j\pi\cos\left(\overline{\vartheta}_{\text{x}}-\alpha\right)},\right.\\&\left.\ldots,e^{j(N_{\text{x}}-1)\pi\cos\left(\overline{\vartheta}_{\text{x}}-\alpha\right)}\right]^{\text{T}}\\&\otimes\left[1,e^{j\pi\sin\left(\overline{\vartheta}_{\text{x}}-\alpha\right)\cos\overline{\vartheta}_{\text{y}}},\right.\\&\left.\ldots,e^{j(N_{\text{y}}-1)\pi\sin\left(\overline{\vartheta}_{\text{x}}-\alpha\right)\cos\overline{\vartheta}_{\text{y}}}\right]^{\text{T}}\end{aligned}\tag{12}$$

$$\begin{aligned}\mathbf{a}_{\text{ARIS}}\left(\vartheta_{\text{x},l}^{(\kappa)},\vartheta_{\text{y},l}^{(\kappa)},\alpha\right)=&\frac{1}{\sqrt{N_{\text{ARIS}}}}\left[1,e^{j\pi\cos\left(\vartheta_{\text{x},l}^{(\kappa)}-\alpha\right)},\right.\\&\left.\ldots,e^{j(N_{\text{x}}-1)\pi\cos\left(\vartheta_{\text{x},l}^{(\kappa)}-\alpha\right)}\right]^{\text{T}}\\&\otimes\left[1,e^{j\pi\sin\left(\vartheta_{\text{x},l}^{(\kappa)}-\alpha\right)\cos\vartheta_{\text{y},l}^{(\kappa)}},\right.\\&\left.\ldots,e^{j(N_{\text{y}}-1)\pi\sin\left(\vartheta_{\text{x},l}^{(\kappa)}-\alpha\right)\cos\vartheta_{\text{y},l}^{(\kappa)}}\right]^{\text{T}}\end{aligned}\tag{13}$$

In Figure 2, the height of the RSU is h_{RSU}, and the height of the ARIS deployment is h_{ARIS}. At discrete time κ, vehicle l has coordinates $x_l^{(\kappa)}$ on the x-axis and $y_l^{(\kappa)}$ on the y-axis. When the ARIS is not rotating, the beam angles in the incident and reflected directions of the ARIS are decomposed into azimuth and pitch angles, which can be defined as respectively:

$$\sin\overline{\vartheta}_{\text{x}}=x_{\text{ARIS}}\left(x_{\text{ARIS}}^2+y_{\text{ARIS}}^2\right)^{-\frac{1}{2}}\tag{14}$$

$$\begin{aligned}\cos\overline{\vartheta}_{\text{y}}=&\left(x_{\text{ARIS}}^2+y_{\text{ARIS}}^2\right)^{\frac{1}{2}}\\&\cdot\left(x_{\text{ARIS}}^2+y_{\text{ARIS}}^2+\left(h_{\text{RSU}}-h_{\text{ARIS}}\right)^2\right)^{-\frac{1}{2}}\end{aligned}\tag{15}$$

$$\sin\vartheta_{\text{x},l}^{(\kappa)}=\left(x_l-x_{\text{ARIS}}\right)\left[\left(x_l-x_{\text{ARIS}}\right)^2+\left(y_l-y_{\text{ARIS}}\right)^2\right]^{-\frac{1}{2}}\tag{16}$$

$$\begin{aligned}\cos\theta_{\text{y},l}^{(\kappa)}=&\left[\left(x_l-x_{\text{ARIS}}\right)^2+\left(y_l-y_{\text{ARIS}}\right)^2\right]^{\frac{1}{2}}\\&\cdot\left[\left(x_l-x_{\text{ARIS}}\right)^2+\left(y_l-y_{\text{ARIS}}\right)^2+h_{\text{ARIS}}^2\right]^{-\frac{1}{2}}\end{aligned}\tag{17}$$

When the RSU communicates with vehicle l over a cascaded channel, if the rotation angle of the ARIS is α, the beam angle ψ_{BS} in the incident direction and the beam angle $\psi_{\text{UE},l}^{(\kappa)}$ in the reflected direction of the ARIS can be expressed by their corresponding azimuth and pitch angles, respectively:

$$\begin{aligned}\psi_{\text{BS}}=&\pi\sin\left(\overline{\vartheta}_{\text{x}}-\alpha\right)\cos\overline{\vartheta}_{\text{y}}\\=&\pi\left(\sin\overline{\vartheta}_{\text{x}}\cos\alpha-\cos\overline{\vartheta}_{\text{x}}\sin\alpha\right)\cos\overline{\vartheta}_{\text{y}}\\=&\pi\left(x_{\text{ARIS}}\cos\alpha-y_{\text{ARIS}}\sin\alpha\right)\\&\left[x_{\text{ARIS}}^2+y_{\text{ARIS}}^2+\left(h_{\text{RSU}}-h_{\text{ARIS}}\right)^2\right]^{-\frac{1}{2}}\end{aligned}\tag{18}$$

$$\begin{aligned}\psi_{\text{UE},l}^{(\kappa)}=&\pi\sin\left(\vartheta_{\text{x},l}^{(\kappa)}-\alpha\right)\cos\vartheta_{\text{y},l}^{(\kappa)}\\=&\pi\left(\sin\vartheta_{\text{x},l}^{(\kappa)}\cos\alpha-\cos\vartheta_{\text{x},l}^{(\kappa)}\sin\alpha\right)\cos\vartheta_{\text{y},l}^{(\kappa)}\\=&\pi\left(\left(x_l-x_{\text{ARIS}}\right)\cos\alpha-\left(y_l-y_{\text{ARIS}}\right)\sin\alpha\right)\\&\times\left[\left(x_l-x_{\text{ARIS}}\right)^2+\left(y_l-y_{\text{ARIS}}\right)^2+h_{\text{ARIS}}^2\right]^{-\frac{1}{2}}\end{aligned}\tag{19}$$

Model the spatial distribution of vehicles on two-lane roads to reflect the traffic distribution. To simplify the research model, it is assumed that vehicles are uniformly distributed in the communication service area, that is, $\mathcal{S}\doteq[-d_{\text{X}},d_{\text{X}}]\times[d_0,d_0+d_{\text{Y}}]$, where d_0 is the distance from the RSU to the lane, and d_{Y} is the width of the total lane. The initial position of the vehicle on axis x follows a uniform distribution $\text{X}\doteq x\sim\text{U}(-d_{\text{X}},d_{\text{X}})$. Therefore, the probability density function of X is:

$$\text{f}_{\text{X}}\left(x\right)=\frac{1}{2d_{\text{X}}}\mathbf{1}_{[-d_{\text{X}},d_{\text{X}}]}\left(x\right)\tag{20}$$

The initial position on axis y follows a uniform distribution $\text{Y}\doteq y\sim\text{U}(d_0,d_0+d_{\text{Y}})$. Then, the probability density function of Y is:

$$\text{f}_{\text{Y}}\left(y\right)=\frac{1}{d_{\text{Y}}}\mathbf{1}_{[d_0,d_0+d_{\text{Y}}]}(y)\tag{21}$$

3. MULTI-VEHICLE BEAM TRACKING BASED ON ARIS ASSISTANCE

3.1. ARIS-Assisted Millimeter-Wave MIMO Beamforming Design

Beamforming is a key technique in MIMO systems for concentrating signal energy in the direction of the target user and mitigating interference from other users. The principle of beamforming technique is to adjust the weighting coefficients of each array element in the antenna array, so as to generate a beam with directionality, in order to achieve the purpose of improving the signal gain. In MIMO systems, beamforming technology not only enables directional signal transmission but also facilitates

spatial multiplexing. Multiple data streams can be simultaneously transmitted to different users within the same frequency band, and system capacity and spectral efficiency are significantly improved.

The optimization problem is modeled next. From Eq. (2), the signal-to-dry noise ratio of the first vehicle is given as:

$$\gamma_l = \frac{\rho_l \left|\mathbf{w}_l^{\mathrm{H}} \mathbf{H}_{\mathrm{BRU},l} \mathbf{f}_l\right|^2}{\sum_{j=1,j\neq l}^{L} \left(\frac{P_j}{\sigma^2}\left(\frac{\lambda}{4\pi d_l}\right)^n\right)\left|\mathbf{w}_l^{\mathrm{H}} \mathbf{H}_{\mathrm{BRU},l} \mathbf{f}_j\right|^2 + 1} \tag{22}$$

Therefore, the signal rate of the lth vehicle is:

$$R_l = \log_2\left(1+\gamma_l\right) \tag{23}$$

The rates discussed in this paper are all rates per unit bandwidth. The sum rate of this multi-vehicle system can be expressed as:

$$R = \sum_{l=1}^{L} R_l = \sum_{l=1}^{L} \log_2\left(1+\gamma_l\right) \tag{24}$$

To improve the beam tracking performance of the system, in this paper, ZF beamforming is selected at the base station end to eliminate the interference between vehicles in Eq. (2). Received signals are linearly processed via ZF beamforming. Through this linear processing, interference is completely eliminated. As a result, the impact of interference on communication quality is greatly reduced, and system performance is thus improved. The main principle of ZF beamforming is to use the pseudo-inverse of the channel matrix to eliminate the interference in the received signal and thus recover the transmitted signal. Define the equivalent channel matrix of the entire BS-ARIS-UE cascade channel as $\boldsymbol{D} = \left[\mathbf{w}_1^{\mathrm{H}}\mathbf{H}_{\mathrm{BRU},1}, \mathbf{w}_2^{\mathrm{H}}\mathbf{H}_{\mathrm{BRU},2}, \ldots, \mathbf{w}_L^{\mathrm{H}}\mathbf{H}_{\mathrm{BRU},L}\right]^{\mathrm{T}}$. The transmitting beamforming matrix at the base station end is given by the following equation:

$$\mathbf{F} = \left[\mathbf{f}_1, \mathbf{f}_2, \ldots, \mathbf{f}_l\right] = \boldsymbol{D}^{\mathrm{H}}\left(\boldsymbol{D}\boldsymbol{D}^{\mathrm{H}}\right)^{-1} \tag{25}$$

After normalization, the transmitting beamforming vector at the base station end about the lth vehicle is obtained as follows:

$$\mathbf{f}_l = \frac{\bar{\mathbf{f}}_l}{\left\|\bar{\mathbf{f}}_l\right\|} \tag{26}$$

where $\bar{\mathbf{f}}_l$ is the lth column of matrix $\mathbf{F}$. Therefore, Eq. (2) can be changed to:

$$r_l = \sqrt{\rho_l}\mathbf{w}_l^{\mathrm{H}}\mathbf{H}_{\mathrm{BRU},l}\mathbf{f}_l s_l + n_l \tag{27}$$

Since the multi-vehicle user interference in Eq. (2) has been eliminated, the signal rate of each vehicle user only depends on its own signal power and noise. Then, according to Eq. (27), the signal rate of the lth vehicle can be obtained as:

$$R_l = \log_2\left(1+\rho_l\left|\mathbf{w}_l^{\mathrm{H}}\mathbf{H}_{\mathrm{BRU},l}\mathbf{f}_l\right|^2\right) = \log_2\left(1+\varpi_l\right) \tag{28}$$

where ϖ_l is the received SNR of the lth vehicle. The sum rate of this ARIS-assisted multi-vehicle system can be expressed as:

$$R = \sum_{l=1}^{L} R_l = \sum_{l=1}^{L} \log_2\left(1+\varpi_l\right) \tag{29}$$

The purpose of this paper is to maximize multi-vehicle and rate R by jointly designing the reflected beamforming matrix $\boldsymbol{\Theta}$ for RIS, the beam merging matrix $\boldsymbol{W} = \mathrm{diag}(\mathbf{w}_1^{\mathrm{H}}, \mathbf{w}_2^{\mathrm{H}}, \ldots, \mathbf{w}_l^{\mathrm{H}})$ for vehicle users, and the rotation angle α for ARIS. Then, the optimization problem for this system can be expressed as:

$$\begin{aligned}
&\mathcal{P}1: \max_{\boldsymbol{W},\boldsymbol{\Theta},\alpha} \sum_{l=1}^{L} \log_2\left(1+\varpi_l\right) \\
&\text{s.t.} \left\|\mathbf{w}_l\right\|^2 = 1, \quad \forall l \in \{1,2,\ldots,L\} \\
&\sum_{l=1}^{L} P_l \leq P \\
&\theta_m \in [0, 2\pi), \quad \forall m \in \{1,2,\ldots,M\} \\
&\xi_m \in [0,1], \quad \forall m \in \{1,2,\ldots,M\} \\
&0 \leq \alpha \leq 2\pi
\end{aligned} \tag{30}$$

where the constraint conditions are in the following order, user-side beam merging vector constraint, transmitting power constraint, the phase constraint of the RIS, the amplitude constraint of the RIS, and the constraint on the rotation angle of the ARIS. This objective function is in the form of logarithmic sums. First, simplify this objective function by introducing an artificial auxiliary variable $\boldsymbol{\lambda} = [\lambda_1, \lambda_2, \ldots, \lambda_L]$. According to the Lagrange duality transformation, the objective function in Eq. (30) can be simplified as:

$$\sum_{l=1}^{L} \log_2\left(1+\varpi_l\right) = \sum_{l=1}^{L} \log\left(1+\lambda_l\right) - \sum_{l=1}^{L}\lambda_l + \sum_{l=1}^{L}\frac{\left(1+\lambda_l\right)\varpi_l}{1+\varpi_l} \tag{31}$$

If $\boldsymbol{\lambda}$ is fixed, then this calculation process transforms the multi-vehicle and rate maximization problem into the SNR maximization problem, that is:

$$\max_{\boldsymbol{W},\boldsymbol{\Theta},\alpha} \sum_{l=1}^{L} \varpi_l \tag{32}$$

To solve the above problems, it is first decomposed into three sub-problems, namely the design sub-problem of beam merging matrix $\boldsymbol{W}$, the design sub-problem of RIS reflection beamforming matrix $\boldsymbol{\Theta}$, and the design sub-problem of ARIS rotation angle α. In IoV scenario, vehicles are in a state of high-speed movement. Therefore, to achieve fast beam alignment, the time overhead caused by computational complexity cannot be ignored. When a single vehicle performs beam tracking, all antenna resources of the RSU are allocated to this vehicle. Therefore, the signal rate of the single vehicle represents the

system optimum. However, when beam tracking is performed for multiple vehicles, two factors must be considered: first, the system sum rate, second, the fairness among vehicles. This is to prevent the performance degradation of edge users. For this purpose, this paper chooses to distribute the power evenly to each user, that is, $P_l = P/L, l \in \{1, 2, \ldots, L\}$.

For the design of the RIS reflection beamforming matrix $\boldsymbol{\Theta}$, given $\boldsymbol{W}$ and α, the optimization problem becomes:

$$\begin{aligned} &\mathcal{P}2: \max_{\boldsymbol{\Theta}} \sum_{l=1}^{L} \varpi_l \\ &s.t. \theta_m \in [-\pi, \pi], \quad \forall m \in \{1, 2, \ldots, M\} \end{aligned} \tag{33}$$

Since RIS employs a UPA, it can be seen from Eq. (12) and Eq. (13) that at the RIS, the array response vectors for incident and reflected directions can be obtained by combining the horizontal and vertical array response vectors via the Kronecker product, respectively. Compared to ULA, UPA generates beamforming with an additional dimension. Therefore, leveraging the inherent Kronecker product structure of UPA, the RIS beamforming design problem can be decomposed into low-dimensional horizontal and vertical subproblems, thereby avoiding the multiplication of large matrices that would arise with an increase in the number of RIS elements [34]. Therefore, this method can significantly reduce the computational complexity and is more suitable for V2I communication scenarios. The overall solution is obtained by solving the unidirectional subproblem and later combining the solutions of the two subproblems using the Kronecker product.

The MIMO channel is decomposed based on the Kronecker product. The ULA response vector at the base station end is first rewritten by mathematical operations:

$$\mathbf{a}_{\mathrm{BS}}(\psi_{\mathrm{BS}}) \doteq \mathbf{a}_{\mathrm{BS,x}}(\psi_{\mathrm{BS}}) \otimes \mathbf{a}_{\mathrm{BS,y}}(\psi_{\mathrm{BS}}) \tag{34}$$

Then, the channel $\mathbf{H}_{\mathrm{BR}}$ from BS to ARIS can be expressed as:

$$\begin{aligned} \mathbf{H}_{\mathrm{BR}} &= \beta_{\mathrm{BR}} \left[\mathbf{a}_{\mathrm{x}}\left(\overline{\vartheta}_{\mathrm{x}}, \alpha\right) \otimes \mathbf{a}_{\mathrm{y}}\left(\overline{\vartheta}_{\mathrm{y}}, \alpha\right)\right] \left[\mathbf{a}_{\mathrm{BS,x}}(\psi_{\mathrm{BS}}) \otimes \mathbf{a}_{\mathrm{BS,y}}(\psi_{\mathrm{BS}})\right]^{\mathrm{H}} \\ &= \beta_{\mathrm{BR}} \left[\mathbf{a}_{\mathrm{x}}\left(\overline{\vartheta}_{\mathrm{x}}, \alpha\right) \mathbf{a}_{\mathrm{BS,x}}^{\mathrm{H}}\left(\psi_{\mathrm{BS}}\right)\right] \otimes \left[\mathbf{a}_{\mathrm{y}}\left(\overline{\vartheta}_{\mathrm{y}}, \alpha\right) \mathbf{a}_{\mathrm{BS,y}}^{\mathrm{H}}(\psi_{\mathrm{BS}})\right] \\ &= \mathbf{H}_{\mathrm{BR,x}} \otimes \mathbf{H}_{\mathrm{BR,y}} \end{aligned} \tag{35}$$

Therefore, channel $\mathbf{H}_{\mathrm{BR}}$ can be composed of two low-dimensional channel components, where $\mathbf{H}_{\mathrm{BR,x}} = \beta_{\mathrm{BR}} \mathbf{a}_{\mathrm{x}}\left(\overline{\vartheta}_{\mathrm{x}}, \alpha\right) \mathbf{a}_{\mathrm{BS,x}}^{\mathrm{H}}(\psi_{\mathrm{BS}})$ is the horizontal channel component, and $\mathbf{H}_{\mathrm{BR,y}} = \mathbf{a}_{\mathrm{y}}(\overline{\vartheta}_{\mathrm{y}}, \alpha) \mathbf{a}_{\mathrm{BS,y}}^{\mathrm{H}}(\psi_{\mathrm{BS}})$ is the vertical channel component. Similarly, the channel $\mathbf{H}_{\mathrm{RU},l}$ from ARIS to UE can be expressed as:

$$\begin{aligned} \mathbf{H}_{\mathrm{RU},l} &= \beta_{\mathrm{RU},l} \left[\mathbf{a}_{\mathrm{UE,x}}\left(\psi_{\mathrm{UE},l}\right) \otimes \mathbf{a}_{\mathrm{UE,y}}\left(\psi_{\mathrm{UE},l}\right)\right] \\ &\quad \left[\mathbf{a}_{\mathrm{x},l}\left(\vartheta_{\mathrm{x},l}, \alpha\right) \otimes \mathbf{a}_{\mathrm{y},l}\left(\vartheta_{\mathrm{y},l}, \alpha\right)\right]^{\mathrm{H}} \\ &= \beta_{\mathrm{RU},l} \left[\mathbf{a}_{\mathrm{UE,x}}\left(\psi_{\mathrm{UE},l}\right) \mathbf{a}_{\mathrm{x},l}^{\mathrm{H}}\left(\vartheta_{\mathrm{x},l}, \alpha\right)\right] \\ &\quad \otimes \left[\mathbf{a}_{\mathrm{UE,y}}\left(\psi_{\mathrm{UE},l}\right) \mathbf{a}_{\mathrm{y},l}^{\mathrm{H}}\left(\vartheta_{\mathrm{y},l}, \alpha\right)\right] \\ &= \mathbf{H}_{l,\mathrm{x}} \otimes \mathbf{H}_{l,\mathrm{y}} \end{aligned} \tag{36}$$

where $\mathbf{H}_{l,\mathrm{x}} = \beta_{\mathrm{RU},l} \mathbf{a}_{\mathrm{UE,x}}(\psi_{\mathrm{UE},l}) \mathbf{a}_{\mathrm{x},l}^{\mathrm{H}}(\vartheta_{\mathrm{x},l}, \alpha)$ and $\mathbf{H}_{l,\mathrm{y}} = \mathbf{a}_{\mathrm{UE,y}}(\psi_{\mathrm{UE},l}) \mathbf{a}_{\mathrm{y},l}^{\mathrm{H}}(\vartheta_{\mathrm{y},l}, \alpha)$ are the horizontal and vertical channel components respectively. According to Eq. (35) and Eq. (36), the received signal can be rewritten as:

$$r_l = \sqrt{\rho_l} \mathbf{w}_l^{\mathrm{H}} \left(\mathbf{H}_{l,\mathrm{x}} \otimes \mathbf{H}_{l,\mathrm{y}}\right) \boldsymbol{\Theta} \left(\mathbf{H}_{\mathrm{BR,x}} \otimes \mathbf{H}_{\mathrm{BR,y}}\right) \mathbf{f}_l s_l + n_l \tag{37}$$

In order to completely decompose the received signal into horizontal and vertical components, the receiver-side beam merging vector $\mathbf{w}_l$, base station-side beamforming vector $\mathbf{f}_l$, and RIS reflection beamforming matrix $\boldsymbol{\Theta}$ are combined by mathematical operations using the Kronecker product structure, respectively, which can be expressed as follows:

$$\mathbf{w}_l \doteq \mathbf{w}_{l,\mathrm{x}} \otimes \mathbf{w}_{l,\mathrm{y}} \tag{38}$$

$$\mathbf{f}_l \doteq \mathbf{f}_{l,\mathrm{x}} \otimes \mathbf{f}_{l,\mathrm{y}} \tag{39}$$

$$\boldsymbol{\Theta} \doteq \boldsymbol{\Theta}_{\mathrm{x}} \otimes \boldsymbol{\Theta}_{\mathrm{y}} \tag{40}$$

Then, Eq. (37) can be expressed as:

$$\begin{aligned} \mathrm{r} &= \sqrt{\rho_l} \mathbf{w}_l^{\mathrm{H}} \left(\mathbf{H}_{l,\mathrm{x}} \otimes \mathbf{H}_{l,\mathrm{y}}\right) \boldsymbol{\Theta} \left(\mathbf{H}_{\mathrm{BR,x}} \otimes \mathbf{H}_{\mathrm{BR,y}}\right) \mathbf{f}_l s_l + n_l \\ &= \sqrt{\rho_l} \left(\mathbf{w}_{l,\mathrm{x}} \otimes \mathbf{w}_{l,\mathrm{y}}\right)^{\mathrm{H}} \left(\mathbf{H}_{l,\mathrm{x}} \otimes \mathbf{H}_{l,\mathrm{y}}\right) \left(\boldsymbol{\Theta}_{\mathrm{x}} \otimes \boldsymbol{\Theta}_{\mathrm{y}}\right) \\ &\quad \left(\mathbf{H}_{\mathrm{BR,x}} \otimes \mathbf{H}_{\mathrm{BR,y}}\right) \left(\mathbf{f}_{l,\mathrm{x}} \otimes \mathbf{f}_{l,\mathrm{y}}\right) s_l + n_l \\ &= \sqrt{\rho_l} \left[\left(\mathbf{w}_{l,\mathrm{x}}^{\mathrm{H}} \mathbf{H}_{l,\mathrm{x}} \boldsymbol{\Theta}_{\mathrm{x}} \mathbf{H}_{\mathrm{BR,x}} \mathbf{f}_{l,\mathrm{x}}\right)\right. \\ &\quad \left. \otimes \left(\mathbf{w}_{l,\mathrm{y}}^{\mathrm{H}} \mathbf{H}_{l,\mathrm{y}} \boldsymbol{\Theta}_{\mathrm{y}} \mathbf{H}_{\mathrm{BR,y}} \mathbf{f}_{l,\mathrm{y}}\right)\right] s_l + n_l \\ &= \sqrt{\rho_l} \left(r_{l,\mathrm{x}} \otimes r_{l,\mathrm{y}}\right) s_l + n_l \end{aligned} \tag{41}$$

where, $r_{l,\mathrm{x}} \doteq \mathbf{w}_{l,\mathrm{x}}^{\mathrm{H}} \mathbf{H}_{l,\mathrm{x}} \boldsymbol{\Theta}_{\mathrm{x}} \mathbf{H}_{\mathrm{BR,x}} \mathbf{f}_{l,\mathrm{x}}$ is the signal component in the horizontal direction and $r_{l,\mathrm{y}} \doteq \mathbf{w}_{l,\mathrm{y}}^{\mathrm{H}} \mathbf{H}_{l,\mathrm{y}} \boldsymbol{\Theta}_{\mathrm{y}} \mathbf{H}_{\mathrm{BR,y}} \mathbf{f}_{l,\mathrm{y}}$ is the signal component in the vertical direction.

Using the decomposed signal model in Eq. (41), solving $\boldsymbol{\Theta}$ is to solve $\boldsymbol{\Theta}_{\mathrm{x}}$ and $\boldsymbol{\Theta}_{\mathrm{y}}$. Meanwhile, maximizing SNR in the horizontal and vertical directions, respectively, is equivalent to maximizing the overall SNR. Then, the complete optimization problem in Eq. (33) can be decomposed into two low-dimensional optimization sub-problems in the horizontal and vertical directions, namely:

$$\begin{aligned} &\mathcal{P}3: \max_{\boldsymbol{\Theta}_{\mathrm{x}}} \sum_{l=1}^{L} \boldsymbol{\varpi}_{l,\mathrm{x}} \\ &\text{s.t. } \theta_{m,\mathrm{x}} \in [0, 2\pi], \quad \forall m \in \{1, 2, \ldots, M_{\mathrm{x}}\} \\ &\xi_{m,\mathrm{x}} \in [0, 1], \quad \forall m \in \{1, 2, \ldots, M_{\mathrm{x}}\} \end{aligned} \tag{42}$$

$$\begin{aligned} &\mathcal{P}4: \max_{\boldsymbol{\Theta}_{\mathrm{y}}} \sum_{l=1}^{L} \varpi_{l,\mathrm{y}} \\ &\text{s.t. } \theta_{m,\mathrm{y}} \in \left[0, 2\pi\right], \quad \forall m \in \left\{1, 2, \ldots, M_{\mathrm{y}}\right\} \\ &\xi_{m,\mathrm{y}} \in \left[0, 1\right], \quad \forall m \in \left\{1, 2, \ldots, M_{\mathrm{y}}\right\} \end{aligned} \tag{43}$$

The solutions to the neutron problems in Eq. (42) and Eq. (43) can be obtained through optimization algorithms. In this paper, the design scheme for RIS terminal reflection beamforming from Reference [35] is adopted. The model is modified according to the research scenario of this paper and subsequently applied to each direction. The specific design process is as follows.

The equivalent channel matrix $\boldsymbol{D}$ of the entire cascaded channel of the BS-ARIS-UE is reconstructed horizontally and vertically:

$$\begin{aligned}\boldsymbol{D}_{\mathrm{q}} &= \boldsymbol{W}\mathbf{h}_{\mathrm{RU,q}}\boldsymbol{\Theta}_{\mathrm{q}}\mathbf{H}_{\mathrm{BR,q}} \\ &= \boldsymbol{W}\mathbf{h}_{\mathrm{RU,q}}\begin{pmatrix}\mathbf{H}^1_{\mathrm{BR,q}} & & \\ & \ddots & \\ & & \mathbf{H}^N_{\mathrm{BR,q}}\end{pmatrix}\begin{pmatrix}\boldsymbol{\Theta}_{\mathrm{q},1}\\ \vdots \\ \boldsymbol{\Theta}_{\mathrm{q},N}\end{pmatrix}\end{aligned} \tag{44}$$

where $\mathbf{H}^n_{\mathrm{BR,q}} = (\mathbf{h}^1_{\mathrm{BR,q}}, \mathbf{h}^2_{\mathrm{BR,q}}, \ldots, \mathbf{h}^M_{\mathrm{BR,q}})$ denotes the nth row vector of the BS-ARIS channel matrix $\mathbf{H}_{\mathrm{BR}}$ satisfying $n \in \{1, 2, \ldots, N\}$. $\boldsymbol{\Theta}_{\mathrm{q,n}} = \mathbf{diag}(\omega_{\mathrm{q,n}}, \omega_{\mathrm{q,n}}, \ldots, \omega_{\mathrm{q,n}})$ is a diagonal array with all the same diagonal elements. In the above notation, $\mathrm{q} \in \{\mathrm{x}, \mathrm{y}\}$ denotes the horizontal or vertical direction; $M \in \{N_{\mathrm{BS,x}}, N_{\mathrm{BS,y}}\}$ represents the number of equivalent horizontal or vertical antennas at the base station end; and $N \in \{N^{\mathrm{x}}_{\mathrm{ARIS}}, N^{\mathrm{y}}_{\mathrm{ARIS}}\}$ denotes the number of equivalent horizontal or vertical elements in ARIS.

Define the matrix $\mathbf{H}_{\mathrm{e,q}}$ to be:

$$\mathbf{H}_{\mathrm{e,q}} = \boldsymbol{W}\mathbf{h}_{\mathrm{RU,q}}\begin{pmatrix}\mathbf{H}^1_{\mathrm{BR,q}} & & \\ & \ddots & \\ & & \mathbf{H}^N_{\mathrm{BR,q}}\end{pmatrix} \tag{45}$$

According to Eq. (45), it can be obtained that:

$$\frac{1}{\lambda_{\mathrm{q}}}\left(\mathbf{H}^{\mathrm{H}}_{\mathrm{e,q}}\mathbf{H}_{\mathrm{e,q}}\right)^{-1} = \mathbf{A}_{\mathrm{q}} = \begin{pmatrix}\mathbf{A}_{\mathrm{q},11} & \mathbf{A}_{\mathrm{q},12} & \cdots & \mathbf{A}_{\mathrm{q},1N} \\ \vdots & \vdots & \ddots & \vdots \\ \mathbf{A}_{\mathrm{q},N1} & \mathbf{A}_{\mathrm{q},N2} & \cdots & \mathbf{A}_{\mathrm{q},NN}\end{pmatrix} \tag{46}$$

where λ_{q} is a normalization factor and is fixed, and $\mathbf{A}_{\mathrm{q,bc}}$ is a diagonal array with all the same diagonal elements and value $\zeta_{\mathrm{q,bc}}$. The following $2N-1$ equation relationship exists:

$$\begin{cases}\boldsymbol{\Theta}_{\mathrm{q},1}\boldsymbol{\Theta}^{\mathrm{H}}_{\mathrm{q},1} = \mathbf{A}_{\mathrm{q},11} \\ \vdots \\ \boldsymbol{\Theta}_{\mathrm{q},N}\boldsymbol{\Theta}^{\mathrm{H}}_{\mathrm{q},N} = \mathbf{A}_{\mathrm{q},NN} \\ \boldsymbol{\Theta}_{\mathrm{q},1}\boldsymbol{\Theta}^{\mathrm{H}}_{\mathrm{q},2} = \mathbf{A}_{\mathrm{q},12} \\ \vdots \\ \boldsymbol{\Theta}_{\mathrm{q},1}\boldsymbol{\Theta}^{\mathrm{H}}_{\mathrm{q},N} = \mathbf{A}_{\mathrm{q},1N}\end{cases} \tag{47}$$

Solving the system of equations yields the diagonal elements of the RIS beamforming matrix $\boldsymbol{\Theta}_{\mathrm{q}}$ in a single direction as:

$$\begin{cases}\xi_{\mathrm{q},1}e^{j\theta_{\mathrm{q},1}} = \sqrt{\zeta_{\mathrm{q},11}} \\ \xi_{\mathrm{q},2}e^{j\theta_{\mathrm{q},2}} = \frac{\zeta^*_{\mathrm{q},12}}{\sqrt{\zeta_{\mathrm{q},11}}} \\ \vdots \\ \xi_{\mathrm{q},N}e^{j\theta_{\mathrm{q},N}} = \frac{\zeta^*_{\mathrm{q},1N}}{\sqrt{\zeta_{\mathrm{q},11}}}\end{cases} \tag{48}$$

In summary, the Kronecker product can be utilized to obtain the complete beamforming matrix $\boldsymbol{\Theta}$ of the RIS as:

$$\begin{aligned}\boldsymbol{\Theta} = \mathbf{diag}\Bigg(&\left(\xi_{\mathrm{x},1}e^{j\theta_{\mathrm{x},1}}, \xi_{\mathrm{x},2}e^{j\theta_{\mathrm{x},2}}, \ldots, \xi_{\mathrm{x},N^{\mathrm{x}}_{\mathrm{ARIS}}}e^{j\theta_{\mathrm{x},N^{\mathrm{x}}_{\mathrm{ARIS}}}}\right) \\ &\otimes\left(\xi_{\mathrm{y},1}e^{j\theta_{\mathrm{y},1}}, \xi_{\mathrm{y},2}e^{j\theta_{\mathrm{y},2}}, \ldots, \xi_{\mathrm{y},N^{\mathrm{y}}_{\mathrm{ARIS}}}e^{j\theta_{\mathrm{y},N^{\mathrm{y}}_{\mathrm{ARIS}}}}\right)\Bigg)\end{aligned} \tag{49}$$

For the user-side beam merging vector $\boldsymbol{W}$, the Singular Value Decomposition (SVD) method is used for the design. Given $\boldsymbol{\Theta}$ and α, since the beam merging vectors are located at the vehicle user end and are independent of each other, the optimization problem in Eq. (32) can be equivalent to the SNR maximization problem for each vehicle user. Then, the optimization problem becomes:

$$\begin{aligned}&\mathcal{P}5: \max_{\mathbf{w}_l} \boldsymbol{\varpi}_l \\ &\text{s.t. } \|\mathbf{w}_l\|^2 = 1, \quad \forall l \in \{1, 2, \ldots, L\}\end{aligned} \tag{50}$$

It is possible to let $\mathbf{H}_{\mathrm{BR}} = \sum_{k=1}^{R_{\mathrm{BR}}} u_{k,\mathrm{BR}}\boldsymbol{\eta}_{k,\mathrm{BR}}\boldsymbol{\nu}^{\mathrm{H}}_{k,\mathrm{BR}}$ and $\mathbf{H}_{\mathrm{RU},l} = \sum_{i=1}^{R_{\mathrm{RU},l}} u_{i,l}\boldsymbol{\eta}_{i,l}\boldsymbol{\nu}^{\mathrm{H}}_{i,l}$ be denoted as the SVD forms of $\mathbf{H}_{\mathrm{BR}}$ and $\mathbf{H}_{\mathrm{RU},l}$, respectively [36], where $R_{\mathrm{BR}} = \mathrm{rank}(\mathbf{H}_{\mathrm{BR}})$; $R_{\mathrm{RU},l} = \mathrm{rank}(\mathbf{H}_{\mathrm{RU},l})$; u are singular values; $\boldsymbol{\eta}$ is the left singular vector; and $\boldsymbol{\nu}$ is the right singular vector.

Since the user terminal typically has limited computational resources and must process dynamic ARIS-UE channel changes caused by high-speed movement in real time, computational complexity must be taken into account. Therefore, adaptive rank reduction is necessary to concentrate beamforming energy on the primary region, achieving a balance between computational complexity and system performance. Dynamic adjustment is carried out based on the power proportion threshold. Assuming that the threshold is χ, then $R_{\mathrm{RU},l}$ is adjusted to $\tilde{R}_{\mathrm{RU},l} = \min\{Y | \sum_{t=1}^{Y}(u_{t,l})^2 / \sum_{t=1}^{R_{\mathrm{RU},l}}(u_{t,l})^2 \geq \chi\}$, that is, the minimum Y is found so that the singular value power proportion exceeds the threshold χ.

Thus, the SNR of the lth vehicle can be obtained as:

$$\begin{aligned}\rho_l\left|\mathbf{w}^{\mathrm{H}}_l\mathbf{H}_{\mathrm{BRU},l}\mathbf{f}_l\right|^2 &= \rho_l\Bigg|\sum_{i=1}^{\tilde{R}_{\mathrm{RU},l}}\sum_{k=1}^{R_{\mathrm{BR}}}u_{i,l}u_{k,\mathrm{BR}} \\ &\quad \mathbf{w}^{\mathrm{H}}_l\boldsymbol{\eta}_{i,l}\boldsymbol{\nu}^{H}_{i,l}\boldsymbol{\Theta}\boldsymbol{\eta}_{k,\mathrm{BR}}\boldsymbol{\nu}^{\mathrm{H}}_{k,\mathrm{BR}}\mathbf{f}_l\Bigg|^2 \\ &\overset{(a)}{\leq} \rho_l\Bigg(\sum_{i=1}^{\tilde{R}_{\mathrm{RU},J}}\sum_{k=1}^{R_{\mathrm{BR}}}u_{i,l}u_{k,\mathrm{BR}} \\ &\quad \left|\mathbf{w}^{\mathrm{H}}_l\boldsymbol{\eta}_{i,l}\right|\left|\boldsymbol{\nu}^{H}_{i,l}\boldsymbol{\Theta}\boldsymbol{\eta}_{k,\mathrm{BR}}\right|\left|\boldsymbol{\nu}^{\mathrm{H}}_{k,\mathrm{BR}}\mathbf{f}_l\right|\Bigg)^2 \\ &\overset{(b)}{\leq} \rho_l\tilde{R}_{\mathrm{RU},l}R_{\mathrm{BR}}\sum_{i=1}^{\tilde{R}_{\mathrm{RU},l}}\sum_{k=1}^{R_{\mathrm{BR}}}u^2_{i,l}u^2_{k,\mathrm{BR}} \\ &\quad \left|\mathbf{w}^{\mathrm{H}}_l\boldsymbol{\eta}_{i,l}\right|^2\left|\boldsymbol{\nu}^{H}_{i,l}\boldsymbol{\Theta}\boldsymbol{\eta}_{k,\mathrm{BR}}\right|^2\left|\boldsymbol{\nu}^{\mathrm{H}}_{k,\mathrm{BR}}\mathbf{f}_l\right|^2\end{aligned} \tag{51}$$

Among them, inequality (a) is due to the triangle inequality, and inequality (b) is due to the Cauchy-Schwarz inequality. In order to design $\mathbf{w}_l$ and thus derive the upper bound of the inequality in Eq. (51), the following lemma is started.

Lemma: For all $k = 1, \ldots, K$, there are $a_k \geqslant 0$ as well as $\varepsilon_k \geqslant 0$. If $\sum_{k=1}^{K} \varepsilon_k \leqslant 1$, $a_{\tilde{k}} \geq a_k$, then $\cdot \sum_{k=1}^{K} a_k \varepsilon_k \leqslant a_{\tilde{k}}$, where $a_{\tilde{k}} = \max(a_1, a_2, \ldots, a_K)$.

Proof: for all $k = 1, \ldots, K$, there is $a_{\tilde{k}} \geq a_k$ such that there exists a nonnegative $\delta_1, \ldots, \delta_K$ and $a_k = a_{\tilde{k}} - \delta_k$. Then, the result follows:

$$\begin{aligned}\sum_{k=1}^{K} a_k \varepsilon_k &= a_{\tilde{k}} \varepsilon_{\tilde{k}} + \sum_{k \neq \tilde{k}}^{K} (a_{\tilde{k}} - \delta_k) \varepsilon_k \\ &= a_{\tilde{k}} \left(\varepsilon_{\tilde{k}} + \sum_{k \neq \tilde{k}}^{K} \varepsilon_k \right) - \sum_{k \neq \tilde{k}}^{K} \delta_k \varepsilon_k \\ &= a_{\tilde{k}} \sum_{k=1}^{K} \varepsilon_k - \sum_{k \neq \tilde{k}}^{K} \delta_k \varepsilon_k \leqslant a_{\tilde{k}} \end{aligned} \tag{52}$$

Since $\sum_{k=1}^{K} \varepsilon_k \leqslant 1$, δ_k and ε_k are nonnegative, then $\sum_{k=1}^{K} a_k \varepsilon_k \leqslant a_{\tilde{k}}$.

The design process of the beam merging vector $\mathbf{w}_l$ for the lth vehicle is as follows. For Eq. (51), ignoring the constant $\rho_l \tilde{R}_{\mathrm{RU},l} R_{\mathrm{BR}}$, the following can be obtained:

$$\sum_{i=1}^{\tilde{R}_{\mathrm{RU},l}} \sum_{k=1}^{R_{\mathrm{BR}}} u_{i,l}^2 u_{k,\mathrm{BR}}^2 \left| \mathbf{w}_l^{\mathrm{H}} \boldsymbol{\eta}_{i,l} \right|^2 \left| \boldsymbol{\nu}_{i,l}^H \boldsymbol{\Theta} \boldsymbol{\eta}_{k,\mathrm{BR}} \right|^2 \left| \boldsymbol{\nu}_{k,\mathrm{BR}}^{\mathrm{H}} \mathbf{f}_l \right|^2$$

$$\leq \sum_{i=1}^{\tilde{R}_{\mathrm{BU},l}} u_{i,l}^2 \left| \mathbf{w}_l^{\mathrm{H}} \boldsymbol{\eta}_{i,l} \right|^2 \sum_{k=1}^{R_{\mathrm{BR}}} u_{k,\mathrm{BR}}^2 \max_{\boldsymbol{\Theta}} \left\{ \left| \boldsymbol{\nu}_{i,l}^H \boldsymbol{\Theta} \boldsymbol{\eta}_{k,\mathrm{BR}} \right|^2 \right\} \left| \boldsymbol{\nu}_{k,\mathrm{BR}}^{\mathrm{H}} \mathbf{f}_l \right|^2 \tag{53}$$

The above inequality holds after taking the maximum value on $\boldsymbol{\Theta}$ such that $\mathrm{g}_i = \sum_{k=1}^{R_{\mathrm{RU},l}} u_{k,\mathrm{BR}}^2 \max_{\boldsymbol{\Theta}} \{ |\boldsymbol{\nu}_{i,l}^H \boldsymbol{\Theta} \rho_{k,\mathrm{BR}}|^2 \} |\boldsymbol{\nu}_{k,\mathrm{BR}}^{\mathrm{H}} \mathbf{f}_l|^2$ and $\mathbf{N} = \max_{\boldsymbol{\Theta}} \{ |\boldsymbol{\nu}_{i,l}^H \boldsymbol{\Theta} \rho_{k,\mathrm{BR}}|^2 \} |\boldsymbol{\nu}_{k,\mathrm{BR}}^{\mathrm{H}} \mathbf{f}_l|^2$.

For any $i = 1, \ldots, \tilde{R}_{\mathrm{RU},l}$, the upper bound of g_i is denoted:

$$\begin{aligned} \mathrm{g}_i &= \sum_{k=1}^{R_{\mathrm{BR}}} u_{k,\mathrm{BR}}^2 \max_{\boldsymbol{\Theta}} \left\{ \left| \boldsymbol{\nu}_{i,l}^H \boldsymbol{\Theta} \boldsymbol{\eta}_{k,\mathrm{BR}} \right|^2 \right\} \left| \boldsymbol{\nu}_{k,\mathrm{BR}}^{\mathrm{H}} \mathbf{f}_l \right|^2 \\ &\leq u_{\tilde{k}(i),\mathrm{BR}}^2 \max_{\boldsymbol{\Theta}} \left\{ \left| \boldsymbol{\nu}_{i,l}^H \boldsymbol{\Theta} \boldsymbol{\eta}_{\tilde{k}(i),\mathrm{BR}} \right|^2 \right\} \left| \boldsymbol{\nu}_{\tilde{k}(i),\mathrm{BR}}^{\mathrm{H}} \mathbf{f}_l \right|^2 \end{aligned} \tag{54}$$

where the above equation is obtained by induction, such that $\mathbf{M} = \max_{\boldsymbol{\Theta}} \{ |\boldsymbol{\nu}_{i,l}^H \boldsymbol{\Theta} \boldsymbol{\eta}_{\tilde{k}(i),\mathrm{BR}}|^2 \} |\boldsymbol{\nu}_{\tilde{k}(i),\mathrm{BR}}^{\mathrm{H}} \mathbf{f}_l|^2$.

Substituting Eq. (53) and Eq. (54) into Eq. (51), the following is obtained:

$$\rho_l \left| \mathbf{w}_l^{\mathrm{H}} \mathbf{H}_{\mathrm{BRU},l} \mathbf{f}_l \right|^2 \leq \rho_l \tilde{R}_{\mathrm{RU},l} R_{\mathrm{BR}} \sum_{i=1}^{\tilde{R}_{\mathrm{RU},l}} u_{i,l}^2 \left| \mathbf{w}_l^{\mathrm{H}} \boldsymbol{\eta}_{i,l} \right|^2$$

$$\left(u_{\tilde{k}(i),\mathrm{BR}}^2 \max_{\boldsymbol{\Theta}} \left\{ \left| \boldsymbol{\nu}_{i,l}^H \boldsymbol{\Theta} \boldsymbol{\eta}_{\tilde{k}(i),\mathrm{BR}} \right|^2 \right\} \left| \boldsymbol{\nu}_{k,\mathrm{BR}}^{\mathrm{H}} \mathbf{f}_l \right|^2 \right)$$

$$\leq \rho_l \tilde{R}_{\mathrm{RU},l} R_{\mathrm{BR}} u_{\tilde{i},l}^2 u_{\tilde{k}(i),\mathrm{BR}}^2$$

$$\left(\max_{\boldsymbol{\Theta}} \left\{ \left| \boldsymbol{\nu}_{i,l}^H \boldsymbol{\Theta} \boldsymbol{\eta}_{\tilde{k}(\tilde{i}),\mathrm{BR}} \right|^2 \right\} \left| \boldsymbol{\nu}_{\tilde{k},\mathrm{BR}}^{\mathrm{H}} \mathbf{f}_l \right|^2 \right)$$

$$= \rho_l \tilde{R}_{\mathrm{RU},l} R_{\mathrm{BR}} u_{\tilde{i},l}^2 u_{\tilde{k}(i),\mathrm{BR}}^2 \bar{\mathrm{M}} \tag{55}$$

where $\bar{\mathrm{M}} = (\max_{\boldsymbol{\Theta}} \{ |\boldsymbol{\nu}_{\tilde{i},l}^H \boldsymbol{\Theta} \boldsymbol{\eta}_{\tilde{k}(\tilde{i}),\mathrm{BR}}|^2 \} |\boldsymbol{\nu}_{\tilde{k},\mathrm{BR}}^{\mathrm{H}} \mathbf{f}_l|^2)$. According to Eq. (26) and Eq. (49), the solutions of $\mathbf{f}_l$ and $\boldsymbol{\Theta}$ have been obtained. The last inequality is due to the normalized vectors $\mathbf{w}_l$ and $\boldsymbol{\eta}_{i,l}$, satisfying $|\mathbf{w}_l^{\mathrm{H}} \boldsymbol{\eta}_{\tilde{i},l}|^2 \leq 1$. $|\mathbf{w}_l^{\mathrm{H}} \boldsymbol{\eta}_{\tilde{i},l}|^2$ denotes the beam merging gain of the beam merging vector $\mathbf{w}_l$ with the channel subspace $\boldsymbol{\eta}_{\tilde{i},l}$. The beam merging gain reaches a maximum value of 1 when $\mathbf{w}_l$ is perfectly aligned with $\boldsymbol{\eta}_{\tilde{i},l}$. At this point $\mathbf{w}_l = \boldsymbol{\eta}_{\tilde{i},l}$, where $\tilde{i} = \mathrm{argmax}_i u_{i,l}^2 u_{\tilde{k}(i),\mathrm{BR}}^2 \mathrm{M}$ and $\tilde{k}(i) = \mathrm{argmax}_k u_{k,\mathrm{BR}}^2 \mathbf{N}$. Additionally, when a vehicle travels continuously at high speed, the SVD method cannot quickly adapt to the dynamic changes of the channel. As a result, beam tracking lag is caused. Therefore, under the adaptive rank reduction mechanism, by integrating prediction vectors to compensate for channel variations, the V2X beam tracking system is enabled to reduce resource consumption while maintaining communication quality, providing an efficient solution for highly dynamic scenarios. The prediction vector is as follows:

$$\mathbf{w}\left(\overline{\psi}_{\mathrm{UE},l}^{(\kappa)}\right) = \frac{1}{\sqrt{N_{\mathrm{UE}}}} \left[1, e^{j\overline{\psi}_{\mathrm{UE},l}^{(\kappa)}}, \ldots, e^{j(N_{\mathrm{UE}}-1)\overline{\psi}_{\mathrm{UE},l}^{(\kappa)}} \right]^{\mathrm{T}} \tag{56}$$

Then for the lth vehicle, the normalized beam merging vector after applying weighted fusion is:

$$\mathbf{w}_l = \frac{\overline{\mathbf{w}}_l}{\|\overline{\mathbf{w}}_l\|} \tag{57}$$

where $\overline{\mathbf{w}}_l = \tau \boldsymbol{\eta}_{\tilde{i},l} + (1-\tau)\mathbf{w}(\bar{\psi}_{\mathrm{UE},l}^{(\kappa)})$, τ are the weights. For the other vehicles, the design process regarding the beam merging vectors is the same as above, then the beam merging matrix $\boldsymbol{W} = \mathrm{diag}(\mathbf{w}_1^{\mathrm{H}}, \mathbf{w}_2^{\mathrm{H}}, \ldots, \mathbf{w}_l^{\mathrm{H}})$.

For the design of the rotation angle α of ARIS, given $\boldsymbol{W}$ and $\boldsymbol{\Theta}$, the optimization problem in Eq. (32) becomes:

$$\begin{aligned} &\mathcal{P}6: \max_{\alpha} \sum_{l=1}^{L} \varpi_l \\ &\text{s.t. } 0 \leq \alpha \leq 2\pi \end{aligned} \tag{58}$$

At this time, since the transmitting beamforming matrix $\boldsymbol{F}$ at the base station end, the reflecting beamforming matrix $\boldsymbol{\Theta}$ of RIS and the beammerging matrix $\boldsymbol{W}$ at the client end are fixed, only the ARIS rotation variable α in the optimization problem of Eq. (58) is considered. The optimal ARIS rotation angle α can be calculated using the fmincon solver from the MATLAB Optimization Toolbox. The fmincon solver is used to find the minimum value of a constrained nonlinear multivariate function. By taking the negative of the objective function, it can

be converted into a maximization problem. The mathematical model of the fmincon solver is generally represented as:

$$\min_{x} f(x)$$
$$s.t. \begin{cases} c(x) \le 0 \\ ceq(x) = 0 \\ A \cdot x \le b \\ Aeq \cdot x = beq \\ lb \le x \le ub \end{cases} \tag{59}$$

where the constraints are, in order, nonlinear inequality constraints, nonlinear equivalence constraints, linear inequality constraints, linear equivalence constraints, and upper and lower bounds on the variables. b and beq are vectors; A and Aeq are matrices; $c(x)$ and $ceq(x)$ are functions that return vectors; $f(x)$ is a function that returns a scalar; and x, lb, and ub can be passed as vectors or matrices. The common format of the fmincon solver is $x = \text{fmincon}(fun, x0, A, b, Aeq, beq, lb, ub, nonlcon)$, where fun denotes the objective function; $x0$ denotes the initial value of x; and $nonlcon$ denotes the nonlinear constraints whose parameter values are typically constraint functions.

3.2. ARIS-Assisted Multi-Vehicle Beam Tracking Algorithm

Suppose that the state information feedback is carried out through the uplink detection signal, or through the existing initial channel access method, RSU can obtain the initial state information of the vehicle, including the initial position and initial speed. Then, focus on the beam tracking after the initial channel access. Meanwhile, in the scenario of the IoV, vehicles can obtain the status information of surrounding vehicles through sensors and Vehicle-to-Vehicle (V2V) communication, and then broadcast the information to the RSU. If the state space model is constructed based on position and velocity, then in discrete time κ, the state vector $\boldsymbol{\mu}_l^{(\kappa)}$ of the lth vehicle can be defined as:

$$\boldsymbol{\mu}_l^{(\kappa)} = \left[x_l^{(\kappa)}, y_l^{(\kappa)}, \nu_l^{(\kappa)}\right]^{\mathrm{T}} \tag{60}$$

The equation of state of the system can be expressed as:

$$\boldsymbol{\mu}_l^{(\kappa)} = \mathbf{A}\boldsymbol{\mu}_l^{(\kappa-1)} + \mathbf{w}_l^{(\kappa-1)} \tag{61}$$

where $\mathbf{w}_l^{(\kappa-1)} \sim \mathcal{CN}(0, \mathbf{Q}_{\omega,l})$ is the error transfer vector at time $\kappa - 1$. According to the change model of vehicle motion, the state transition matrix can be expressed as:

$$\mathbf{A}_l = \begin{bmatrix} 1 & 0 & T_s \cos\varphi_l \\ 0 & 1 & T_s \sin\varphi_l \\ 0 & 0 & 1 \end{bmatrix} \tag{62}$$

The covariance matrix $\mathbf{Q}_{\omega,l}$ of the error transition vector is expressed as:

$$\mathbf{Q}_{\omega,l} = \text{diag}\left[T_s^2\sigma_{\omega,l}^2\cos^2\varphi_l, T_s^2\sigma_{\omega,l}^2\sin^2\varphi_l, \sigma_{\omega,l}^2\right] \tag{63}$$

where $\varphi_l \in [-\pi/2, \pi/2]$ is the steering angle of the lth vehicle; T_s is the measurement cycle; and $\sigma_{\omega,l}^2$ is the variance of the speed error parameter. The speed error parameter is the assumed noise, which is used to represent the change of vehicle speed [37].

In the communication process, since the BS and ARIS are deployed in fixed positions, and the vehicle user is in motion, β_{BR} and ψ_{BS} are fixed values while $\beta_{\text{RU},l}^{(\kappa)}$ and $\psi_{\text{UE},l}^{(\kappa)}$ are time-varying values in the channel. Taking the received signal $r_l^{(\kappa)}$ as the system observation equation, Eq. (27) can be reexpressed as follows:

$$r_l^{(\kappa)} = \sqrt{\rho_l^{(\kappa)}}\beta_{\text{RU},l}\left(d_{\text{RU},l}^{(\kappa)}\right)\mathbf{t}_l\left(\psi_{\text{UE},l}^{(\kappa)}\right) + n_l^{(\kappa)} \tag{64}$$

In order to facilitate the state prediction and correction process in the same domain, Eq. (64) is rewritten in the real number domain, namely:

$$\tilde{\mathbf{r}}_l^{(\kappa)} = \sqrt{\rho_l^{(\kappa)}}\tilde{\beta}_{\text{RU},l}\left(d_{\text{RU},l}^{(\kappa)}\right)\tilde{\mathbf{t}}_l\left(\psi_{\text{UE},l}^{(\kappa)}\right) + \tilde{\mathbf{n}}_l^{(\kappa)} \tag{65}$$

where all variables contained in Eq. (65) are rerepresented in the real field as follows:

$$\tilde{\mathbf{r}}_l^{(\kappa)} = \left[r_l^{(\kappa),\text{re}}, r_l^{(\kappa),\text{im}}\right]^{\mathrm{T}} \tag{66}$$

$$\tilde{\beta}_{\text{RU},l}^{(\kappa)} = \begin{bmatrix} \beta_{\text{RU},l}^{\text{re}}\left(d_{\text{RU},l}^{(\kappa)}\right) & -\beta_{\text{RU},l}^{\text{im}}\left(d_{\text{RU},l}^{(\kappa)}\right) \\ \beta_{\text{RU},l}^{\text{im}}\left(d_{\text{RU},l}^{(\kappa)}\right) & \beta_{\text{RU},l}^{\text{re}}\left(d_{\text{RU},l}^{(\kappa)}\right) \end{bmatrix} \tag{67}$$

$$\tilde{\mathbf{t}}_l\left(\psi_{\text{UE},l}^{(\kappa)}\right) = \left[\mathbf{t}_l^{\text{re}}\left(\psi_{\text{UE},l}^{(\kappa)}\right), \mathbf{t}_l^{\text{im}}\left(\psi_{\text{UE},l}^{(\kappa)}\right)\right]^{\mathrm{T}} \tag{68}$$

$$\tilde{\mathbf{n}}_l^{(\kappa)} = \left[n_l^{(\kappa),\text{re}}, n_l^{(\kappa),\text{im}}\right]^{\mathrm{T}} \tag{69}$$

According to Eq. (19), the function $\psi_{\text{UE},l}^{(\kappa)}$ of the beam direction from ARIS to the lth UE reflection path at time κ is defined as a function of the state vector, that is:

$$\begin{aligned} \psi_{\text{UE},l}^{(\kappa)} &= \pi\left((x_l - x_{\text{ARIS}})\cos\alpha - (y_l - y_{\text{ARIS}})\sin\alpha\right) \\ &\quad \times \left[(x_l - x_{\text{ARIS}})^2 + (y_l - y_{\text{ARIS}})^2 + h_{\text{ARIS}}^2\right]^{-\frac{1}{2}} \\ &\doteq \mathrm{g}_l\left(\boldsymbol{\mu}_l^{(\kappa)}\right) \end{aligned} \tag{70}$$

Similarly, the distance $d_{\text{RU},l}^{(\kappa)}$ between the ARIS and the lth vehicle can be defined as a function of the state vector, that is:

$$d_{\text{RU},l}^{(\kappa)} = \left[(x_l - x_{\text{RIS}})^2 + (y_l - y_{\text{RIS}})^2 + h_{\text{RIS}}^2\right]^{\frac{1}{2}} \doteq \mathrm{g}_{\text{RU},l}\left(\boldsymbol{\mu}_l^{(\kappa)}\right) \tag{71}$$

At this point, Eq. (65) can be reexpressed as a function related to $\mathrm{g}(\boldsymbol{\mu}^{(\kappa)})$:

$$\tilde{\mathbf{r}}^{(\kappa)} = \sqrt{\rho_l^{(\kappa)}}\tilde{\beta}_{\text{RU},l}\left(\mathrm{g}_{\text{RU},l}\left(\boldsymbol{\mu}_l^{(\kappa)}\right)\right)\tilde{\mathbf{t}}_l\left(\mathrm{g}_l\left(\boldsymbol{\mu}_l^{(\kappa)}\right)\right) + \tilde{\mathbf{n}}_l^{(\kappa)}$$

$$= \sqrt{\rho_l^{(\kappa)}}\tilde{\mathbf{h}}_l\left(\boldsymbol{\mu}_l^{(\kappa)}\right) + \tilde{\mathbf{n}}_l^{(\kappa)} \tag{72}$$

In summary, the channel vector can be expressed as:

$$\begin{aligned}\tilde{\mathbf{h}}_l\left(\boldsymbol{\mu}^{(\kappa)}\right) &= \begin{bmatrix}\mathbf{h}_l^{\mathrm{re}}\left(\boldsymbol{\mu}(\kappa)\right)\\ \mathbf{h}_l^{\mathrm{im}}\left(\boldsymbol{\mu}^{(\kappa)}\right)\end{bmatrix}\\ &= \begin{bmatrix}\beta_{\mathrm{RU},l}^{\mathrm{re}}\left(\mathrm{g}_{\mathrm{RU},l}\left(\boldsymbol{\mu}_l^{(\kappa)}\right)\right)\mathbf{t}_l^{\mathrm{re}}\left(\mathrm{g}_l\left(\boldsymbol{\mu}_l^{(\kappa)}\right)\right) - \beta_{\mathrm{RU},l}^{\mathrm{im}}\left(\mathrm{g}_{\mathrm{RU},l}\left(\boldsymbol{\mu}_l^{(\kappa)}\right)\right)\mathbf{t}_l^{\mathrm{im}}\left(\mathrm{g}_l\left(\boldsymbol{\mu}_l^{(\kappa)}\right)\right)\\ \beta_{\mathrm{RU},l}^{\mathrm{im}}\left(\mathrm{g}_{\mathrm{RU},l}\left(\boldsymbol{\mu}_l^{(\kappa)}\right)\right)\mathbf{t}_l^{\mathrm{re}}\left(\mathrm{g}_l\left(\boldsymbol{\mu}_l^{(\kappa)}\right)\right) + \beta_{\mathrm{RU},l}^{\mathrm{re}}\left(\mathrm{g}_{\mathrm{RU},l}\left(\boldsymbol{\mu}_l^{(\kappa)}\right)\right)\mathbf{t}_l^{\mathrm{im}}\left(\mathrm{g}_l\left(\boldsymbol{\mu}_l^{(\kappa)}\right)\right)\end{bmatrix}\end{aligned} \tag{73}$$

Then, the first-order Taylor series approximation of the channel vector $\tilde{\mathbf{h}}_l$ obtained from the predicted state vector $\hat{\boldsymbol{\mu}}_l^{(\kappa|\kappa-1)}$ at the moment κ is:

$$\tilde{\mathbf{h}}_l\left(\boldsymbol{\mu}_l^{(\kappa)}\right) \simeq \tilde{\mathbf{h}}_l\left(\hat{\boldsymbol{\mu}}_l^{(\kappa|\kappa-1)}\right) + \tilde{\mathbf{G}}_l^{(\kappa|\kappa-1)}\left(\boldsymbol{\mu}_l^{(\kappa)} - \hat{\boldsymbol{\mu}}_l^{(\kappa|\kappa-1)}\right) \tag{74}$$

The received signal in Eq. (72) can be approximately expressed as:

$$\begin{aligned}\tilde{\mathbf{r}}_l^{(\kappa)} \simeq\ & \sqrt{\rho_l^{(\kappa)}}\tilde{\mathbf{h}}_l\left(\hat{\boldsymbol{\mu}}^{(\kappa|\kappa-1)}\right) + \sqrt{\rho_l^{(\kappa)}}\mathbf{G}_l^{(\kappa|\kappa-1)}\\ & \left(\boldsymbol{\mu}^{(\kappa)} - \hat{\boldsymbol{\mu}}^{(\kappa|\kappa-1)}\right) + \tilde{\mathbf{n}}_l^{(\kappa)}\end{aligned} \tag{75}$$

where $\hat{\boldsymbol{\mu}}_l^{(\kappa|\kappa-1)}$ is an estimate based on the observation vector $\boldsymbol{\mu}_l^{(\kappa)}$ at moment $\kappa-1$, and $\tilde{\mathbf{G}}_l^{(\kappa|\kappa-1)}$ is the Jacobi matrix, denoted as:

$$\tilde{\mathbf{G}}_l^{(\kappa|\kappa-1)} = \left[\dot{\mathbf{h}}_l^{\mathrm{re}}\left(\hat{\boldsymbol{\mu}}_l^{(\kappa|\kappa-1)}\right), \dot{\mathbf{h}}_l^{\mathrm{im}}\left(\hat{\boldsymbol{\mu}}_l^{(\kappa|\kappa-1)}\right)\right]^{\mathrm{T}} \tag{76}$$

The terms of equation are denoted as:

$$\begin{aligned}\dot{\mathbf{h}}_l^{\mathrm{re}}\left(\hat{\boldsymbol{\mu}}_l^{(\kappa|\kappa-1)}\right) \doteq\ & \dot{\beta}_{\mathrm{RU},l}^{\mathrm{re}}\left(\mathrm{g}_{\mathrm{RU},l}\left(\boldsymbol{\mu}_l^{(\kappa)}\right)\right)\dot{\mathbf{t}}_l^{\mathrm{re}}\left(\mathrm{g}_l\left(\hat{\boldsymbol{\mu}}_l^{(\kappa|\kappa-1)}\right)\right)\dot{\mathrm{g}}_l\left(\hat{\boldsymbol{\mu}}_l^{(\kappa|\kappa-1)}\right)\\ & + \dot{\beta}_{\mathrm{RU},l}^{\mathrm{re}}\left(\mathrm{g}_{\mathrm{RU},l}\left(\boldsymbol{\mu}_l^{(\kappa)}\right)\right)\dot{\mathrm{g}}_{\mathrm{RU},l}\left(\boldsymbol{\mu}_l^{(\kappa)}\right)\mathbf{t}_l^{\mathrm{re}}\left(\mathrm{g}_l\left(\hat{\boldsymbol{\mu}}_l^{(\kappa|\kappa-1)}\right)\right)\\ & - \dot{\beta}_{\mathrm{RU},l}^{\mathrm{im}}\left(\mathrm{g}_{\mathrm{RU},l}\left(\boldsymbol{\mu}_l^{(\kappa)}\right)\right)\dot{\mathbf{t}}_l^{\mathrm{im}}\left(\mathrm{g}_l\left(\hat{\boldsymbol{\mu}}_l^{(\kappa|\kappa-1)}\right)\right)\dot{\mathrm{g}}_l\left(\hat{\boldsymbol{\mu}}_l^{(\kappa|\kappa-1)}\right)\\ & - \dot{\beta}_{\mathrm{RU},l}^{\mathrm{im}}\left(\mathrm{g}_{\mathrm{RU},l}\left(\boldsymbol{\mu}_l^{(\kappa)}\right)\right)\dot{\mathrm{g}}_{\mathrm{RU},l}\left(\boldsymbol{\mu}_l^{(\kappa)}\right)\mathbf{t}_l^{\mathrm{im}}\left(\mathrm{g}_l\left(\hat{\boldsymbol{\mu}}_l^{(\kappa|\kappa-1)}\right)\right)\\ \dot{\mathbf{h}}_l^{\mathrm{im}}\left(\hat{\boldsymbol{\mu}}_l^{(\kappa|\kappa-1)}\right) \doteq\ & \dot{\beta}_{\mathrm{RU},l}^{\mathrm{im}}\left(\mathrm{g}_{\mathrm{RU},l}\left(\boldsymbol{\mu}_l^{(\kappa)}\right)\right)\dot{\mathbf{t}}_l^{\mathrm{re}}\left(\mathrm{g}_l\left(\hat{\boldsymbol{\mu}}_l^{(\kappa|\kappa-1)}\right)\right)\dot{\mathrm{g}}_l\left(\hat{\boldsymbol{\mu}}_l^{(\kappa|\kappa-1)}\right)\\ & + \dot{\beta}_{\mathrm{RU},l}^{\mathrm{im}}\left(\mathrm{g}_{\mathrm{RU},l}\left(\boldsymbol{\mu}_l^{(\kappa)}\right)\right)\dot{\mathrm{g}}_{\mathrm{RU},l}\left(\boldsymbol{\mu}_l^{(\kappa)}\right)\mathbf{t}_l^{\mathrm{re}}\left(\mathrm{g}_l\left(\hat{\boldsymbol{\mu}}_l^{(\kappa|\kappa-1)}\right)\right)\\ & + \beta_{\mathrm{RU},l}^{\mathrm{re}}\left(\mathrm{g}_{\mathrm{RU},l}\left(\boldsymbol{\mu}_l^{(\kappa)}\right)\right)\dot{\mathbf{t}}_l^{\mathrm{im}}\left(\mathrm{g}_l\left(\hat{\boldsymbol{\mu}}_l^{(\kappa|\kappa-1)}\right)\right)\dot{\mathrm{g}}_l\left(\hat{\boldsymbol{\mu}}_l^{(\kappa|\kappa-1)}\right)\\ & + \dot{\beta}_{\mathrm{RU},l}^{\mathrm{re}}\left(\mathrm{g}_{\mathrm{RU},l}\left(\boldsymbol{\mu}_l^{(\kappa)}\right)\right)\dot{\mathrm{g}}_{\mathrm{RU},l}\left(\boldsymbol{\mu}_l^{(\kappa)}\right)\mathbf{t}_l^{\mathrm{im}}\left(\mathrm{g}_l\left(\hat{\boldsymbol{\mu}}_l^{(\kappa|\kappa-1)}\right)\right)\end{aligned} \tag{77}$$

$$\begin{aligned}\dot{\mathbf{h}}_l^{\mathrm{re}}\left(\hat{\boldsymbol{\mu}}_l^{(\kappa|\kappa-1)}\right) \doteq\ & \dot{\beta}_{\mathrm{RU},l}^{\mathrm{re}}\left(\mathrm{g}_{\mathrm{RU},l}\left(\boldsymbol{\mu}_l^{(\kappa)}\right)\right)\dot{\mathbf{t}}_l^{\mathrm{re}}\left(\mathrm{g}_l\left(\hat{\boldsymbol{\mu}}_l^{(\kappa|\kappa-1)}\right)\right)\dot{\mathrm{g}}_l\left(\hat{\boldsymbol{\mu}}_l^{(\kappa|\kappa-1)}\right)\\ & + \dot{\beta}_{\mathrm{RU},l}^{\mathrm{re}}\left(\mathrm{g}_{\mathrm{RU},l}\left(\boldsymbol{\mu}_l^{(\kappa)}\right)\right)\dot{\mathrm{g}}_{\mathrm{RU},l}\left(\boldsymbol{\mu}_l^{(\kappa)}\right)\mathbf{t}_l^{\mathrm{re}}\left(\mathrm{g}_l\left(\hat{\boldsymbol{\mu}}_l^{(\kappa|\kappa-1)}\right)\right)\\ & - \dot{\beta}_{\mathrm{RU},l}^{\mathrm{im}}\left(\mathrm{g}_{\mathrm{RU},l}\left(\boldsymbol{\mu}_l^{(\kappa)}\right)\right)\dot{\mathbf{t}}_l^{\mathrm{im}}\left(\mathrm{g}_l\left(\hat{\boldsymbol{\mu}}_l^{(\kappa|\kappa-1)}\right)\right)\dot{\mathrm{g}}_l\left(\hat{\boldsymbol{\mu}}_l^{(\kappa|\kappa-1)}\right)\\ & - \dot{\beta}_{\mathrm{RU},l}^{\mathrm{im}}\left(\mathrm{g}_{\mathrm{RU},l}\left(\boldsymbol{\mu}_l^{(\kappa)}\right)\right)\dot{\mathrm{g}}_{\mathrm{RU},l}\left(\boldsymbol{\mu}_l^{(\kappa)}\right)\mathbf{t}_l^{\mathrm{im}}\left(\mathrm{g}_l\left(\hat{\boldsymbol{\mu}}_l^{(\kappa|\kappa-1)}\right)\right)\\ \dot{\mathbf{h}}_l^{\mathrm{im}}\left(\hat{\boldsymbol{\mu}}_l^{(\kappa|\kappa-1)}\right) \doteq\ & \dot{\beta}_{\mathrm{RU},l}^{\mathrm{im}}\left(\mathrm{g}_{\mathrm{RU},l}\left(\boldsymbol{\mu}_l^{(\kappa)}\right)\right)\dot{\mathbf{t}}_l^{\mathrm{re}}\left(\mathrm{g}_l\left(\hat{\boldsymbol{\mu}}_l^{(\kappa|\kappa-1)}\right)\right)\dot{\mathrm{g}}_l\left(\hat{\boldsymbol{\mu}}_l^{(\kappa|\kappa-1)}\right)\\ & + \dot{\beta}_{\mathrm{RU},l}^{\mathrm{im}}\left(\mathrm{g}_{\mathrm{RU},l}\left(\boldsymbol{\mu}_l^{(\kappa)}\right)\right)\dot{\mathrm{g}}_{\mathrm{RU},l}\left(\boldsymbol{\mu}_l^{(\kappa)}\right)\mathbf{t}_l^{\mathrm{re}}\left(\mathrm{g}_l\left(\hat{\boldsymbol{\mu}}_l^{(\kappa|\kappa-1)}\right)\right)\\ & + \beta_{\mathrm{RU},l}^{\mathrm{re}}\left(\mathrm{g}_{\mathrm{RU},l}\left(\boldsymbol{\mu}_l^{(\kappa)}\right)\right)\dot{\mathbf{t}}_l^{\mathrm{im}}\left(\mathrm{g}_l\left(\hat{\boldsymbol{\mu}}_l^{(\kappa|\kappa-1)}\right)\right)\dot{\mathrm{g}}_l\left(\hat{\boldsymbol{\mu}}_l^{(\kappa|\kappa-1)}\right)\\ & + \dot{\beta}_{\mathrm{RU},l}^{\mathrm{re}}\left(\mathrm{g}_{\mathrm{RU},l}\left(\boldsymbol{\mu}_l^{(\kappa)}\right)\right)\dot{\mathrm{g}}_{\mathrm{RU},l}\left(\boldsymbol{\mu}_l^{(\kappa)}\right)\mathbf{t}_l^{\mathrm{im}}\left(\mathrm{g}_l\left(\hat{\boldsymbol{\mu}}_l^{(\kappa|\kappa-1)}\right)\right)\end{aligned} \tag{78}$$

where the derivatives of the distance function and beam direction function from ARIS to vehicle l are shown as follows:

$$\begin{aligned}&\dot{\mathrm{g}}_{\mathrm{RU},l}(\boldsymbol{\mu}^{(\kappa)})\\ &\doteq \frac{\left[\hat{x}_l^{(\kappa|\kappa-1)} - x_{\mathrm{ARIS}},\ \hat{\mathrm{y}}_l^{(\kappa|\kappa-1)} - y_{\mathrm{ARIS}},\ \cos\varphi_l(\hat{x}_l^{(\kappa|\kappa-1)} - x_{\mathrm{ARIS}})T_s\right]}{\left[\left(\hat{x}_l^{(\kappa|\kappa-1)} - x_{\mathrm{ARIS}}\right)^2 + \left(\hat{\mathrm{y}}_l^{(\kappa|\kappa-1)} - y_{\mathrm{ARIS}}\right)^2 + h_{\mathrm{ARIS}}^2\right]^{1/2}}\end{aligned} \tag{79}$$

$$\begin{aligned}&\dot{\mathrm{g}}_l\left(\hat{\boldsymbol{\mu}}^{(\kappa|\kappa-1)}\right)\\ &\doteq \frac{\pi\begin{bmatrix}\left(\hat{\mathrm{y}}_l^{(\kappa|\kappa-1)} - y_{\mathrm{ARIS}}\right)\left(\left(\hat{\mathrm{y}}_l^{(\kappa|\kappa-1)} - y_{\mathrm{ARIS}}\right)\cos\alpha + \left(\hat{x}_l^{(\kappa|\kappa-1)} - x_{\mathrm{ARIS}}\right)\sin\alpha\right) + h_{\mathrm{ARIS}}^2\cos\alpha\\ -\left(\hat{x}_l^{(\kappa|\kappa-1)} - x_{\mathrm{ARIS}}\right)\left(\left(\hat{x}_l^{(\kappa|\kappa-1)} - x_{\mathrm{ARIS}}\right)\sin\alpha + \left(\hat{\mathrm{y}}_l^{(\kappa|\kappa-1)} - y_{\mathrm{ARIS}}\right)\cos\alpha\right) + h_{\mathrm{ARIS}}^2\sin\alpha\\ cos\varphi\left[\left(\hat{\mathrm{y}}_l^{(\kappa|\kappa-1)} - y_{\mathrm{ARIS}}\right)\left(\left(\hat{\mathrm{y}}_l^{(\kappa|\kappa-1)} - y_{\mathrm{ARIS}}\right)\cos\alpha + \left(\hat{x}_l^{(\kappa|\kappa-1)} - x_{\mathrm{ARIS}}\right)\sin\alpha\right) + h_{\mathrm{ARIS}}^2\cos\alpha\right]T_s\end{bmatrix}^{\mathrm{T}}}{\left[\left(\hat{x}_l^{(\kappa|\kappa-1)} - x_{\mathrm{ARIS}}\right)^2 + \left(\hat{\mathrm{y}}_l^{(\kappa|\kappa-1)} - y_{\mathrm{ARIS}}\right)^2 + h_{\mathrm{ARIS}}^2\right]^{\frac{3}{2}}}\end{aligned} \tag{80}$$

Let the Jacobi matrix $\tilde{\mathbf{G}} = \mathrm{diag}\left(\tilde{\mathbf{G}}_1, \tilde{\mathbf{G}}_2, \ldots, \tilde{\mathbf{G}}_L\right)$, state vector $\hat{\boldsymbol{\mu}} = \left[\hat{\boldsymbol{\mu}}_1^{\mathrm{T}}, \hat{\boldsymbol{\mu}}_2^{\mathrm{T}}, \ldots, \hat{\boldsymbol{\mu}}_L^{\mathrm{T}}\right]^{\mathrm{T}}$, received signal $\tilde{\mathbf{r}} = \left[\tilde{\mathbf{r}}_1^{\mathrm{T}}, \tilde{\mathbf{r}}_2^{\mathrm{T}}, \ldots, \tilde{\mathbf{r}}_L^{\mathrm{T}}\right]^{\mathrm{T}}$, state transfer matrix $\mathbf{A} = \mathrm{diag}\left(\mathbf{A}_1, \mathbf{A}_2, \ldots, \mathbf{A}_L\right)$, and covariance matrix $\mathbf{Q}_\omega = \mathrm{diag}\left(\mathbf{Q}_{\omega,1}, \mathbf{Q}_{\omega,2}, \ldots, \mathbf{Q}_{\omega,L}\right)$ of the error transfer vector, the specific procedure of the EKF-based beam tracking algorithm under multi-vehicle is shown as follows:

(1) State prediction update

$$\hat{\boldsymbol{\mu}}^{(\kappa|\kappa-1)} = \mathbf{A}\hat{\boldsymbol{\mu}}^{(\kappa-1|\kappa-1)} \tag{81}$$

(2) Compute a priori covariance matrix

$$\mathbf{P}^{(\kappa|\kappa-1)} = \mathbf{A}\mathbf{P}^{(\kappa-1|\kappa-1)}\mathbf{A}^{\mathrm{T}} + \mathbf{Q}_\omega \tag{82}$$

(3) Kalman gain matrix update

$$\begin{aligned}\mathbf{K}^{(\kappa)} =\ & \mathbf{P}^{(\kappa|\kappa-1)}\left((\boldsymbol{\rho}^{(\kappa)} \otimes \mathbf{I}_2)\tilde{\mathbf{G}}^{(\kappa|\kappa-1)}\right)^{\mathrm{T}}\\ & \times \left((\boldsymbol{\rho}^{(\kappa)} \otimes \mathbf{I}_2)\tilde{\mathbf{G}}^{(\kappa|\kappa-1)}\mathbf{P}^{(\kappa|\kappa-1)}\right.\\ & \left.\left((\boldsymbol{\rho}^{(\kappa)} \otimes \mathbf{I}_2)\tilde{\mathbf{G}}^{(\kappa|\kappa-1)}\right)^{\mathrm{T}} + \frac{\mathbf{I}_{2L}}{2}\right)^{-1}\end{aligned} \tag{83}$$

where $\boldsymbol{\rho}^{(\kappa)} = \mathrm{diag}([\sqrt{\rho_1^{(\kappa)}}, \sqrt{\rho_2^{(\kappa)}}, \ldots, \sqrt{\rho_l^{(\kappa)}}])$, $\mathbf{K}^{(\kappa)}$ are Kalman gain matrices and $\mathbf{I}$ represents the unit matrix.

(4) Update system state estimate a posteriori

$$\hat{\boldsymbol{\mu}}^{(\kappa|\kappa)} = \hat{\boldsymbol{\mu}}^{(\kappa|\kappa-1)} + \mathbf{K}^{(\kappa)}\left(\tilde{\mathbf{r}}^{(\kappa)} - \left(\boldsymbol{\rho}^{(\kappa)} \otimes \mathbf{I}_2\right)\tilde{\mathbf{h}}\left(\hat{\boldsymbol{\mu}}^{(\kappa|\kappa-1)}\right)\right) \tag{84}$$

where $\tilde{\mathbf{h}}(\hat{\boldsymbol{\mu}}^{(\kappa|\kappa-1)}) = [(\tilde{\mathbf{h}}_1(\hat{\boldsymbol{\mu}}^{(\kappa|\kappa-1)}))^{\mathrm{T}}, (\tilde{\mathbf{h}}_2(\hat{\boldsymbol{\mu}}^{(\kappa|\kappa-1)}))^{\mathrm{T}}, \ldots, (\tilde{\mathbf{h}}_l(\hat{\boldsymbol{\mu}}^{(\kappa|\kappa-1)}))^{\mathrm{T}}]^{\mathrm{T}}$ is the channel vector.

(5) Update a posteriori covariance matrix

$$\mathbf{P}^{(\kappa|\kappa)} = \left(\mathbf{I}_{3L} - \mathbf{K}^{(\kappa)}\left(\boldsymbol{\rho}^{(\kappa)} \otimes \mathbf{I}_2\right)\tilde{\mathbf{G}}^{(\kappa|\kappa-1)}\right)\mathbf{p}^{(\kappa|\kappa-1)} \tag{85}$$

The above is done in one round of iteration. By iterating continuously, we can find the system state estimation value needed at each moment, including the position and speed information of each vehicle.

When the vehicle is driving at a high speed, frequent beam switching or channel estimation will lead to beam tracking lag, a sharp decrease in the quality of the received signal, and communication interruption. In addition, the linear approximation of the EKF algorithm inevitably introduces an estimation error, and the estimation error becomes progressively larger with time, which leads to a significant degradation of the system

TABLE 1. Multi-vehicle EKF beam tracking algorithm based on angular deviation correction mechanism.

Algorithm 1: Multi-vehicle EKF beam tracking algorithm based on angular deviation correction mechanism
Initialize: Number of time slots T, covariance matrix $\mathbf{P}^{(0)}=\mathbf{0}_{3L\times 3L}$, state vector $\hat{\boldsymbol{\mu}}^{(0)}=\boldsymbol{\mu}^{(0)}+e_{\varepsilon}$
for $t=0$ to T **do**
State prediction update: $\hat{\boldsymbol{\mu}}^{(\kappa\mid\kappa-1)}=\mathbf{A}\hat{\boldsymbol{\mu}}^{(\kappa-1\mid\kappa-1)}$
Calculate a priori covariance matrix: $\mathbf{P}^{(\kappa\mid\kappa-1)}=\mathbf{A}\mathbf{P}^{(\kappa-1\mid\kappa-1)}\mathbf{A}^{\mathrm{T}}+\mathbf{Q}_{\omega}$
Kalman gain matrix update:
$\mathbf{K}^{(\kappa)}=\mathbf{P}^{(\kappa\mid\kappa-1)}\left(\left(\boldsymbol{\rho}^{(\kappa)}\otimes\mathbf{I}_2\right)\tilde{\mathbf{G}}^{(\kappa\mid\kappa-1)}\right)^{\mathrm{T}}\left(\left(\boldsymbol{\rho}^{(\kappa)}\otimes\mathbf{I}_2\right)\tilde{\mathbf{G}}^{(\kappa\mid\kappa-1)}\mathbf{P}^{(\kappa\mid\kappa-1)}\left(\left(\boldsymbol{\rho}^{(\kappa)}\otimes\mathbf{I}_2\right)\tilde{\mathbf{G}}^{(\kappa\mid\kappa-1)}\right)^{\mathrm{T}}+\frac{\mathbf{I}_{2L}}{2}\right)^{-1}$
Update system state estimate a posteriori: $\hat{\boldsymbol{\mu}}^{(\kappa\mid\kappa)}=\hat{\boldsymbol{\mu}}^{(\kappa\mid\kappa-1)}+\mathbf{K}^{(\kappa)}\left(\tilde{\mathbf{r}}^{(\kappa)}-\left(\boldsymbol{\rho}^{(\kappa)}\otimes\mathbf{I}_2\right)\tilde{\mathbf{h}}\left(\hat{\boldsymbol{\mu}}^{(\kappa\mid\kappa-1)}\right)\right)$
Update a posteriori covariance matrix: $\mathbf{P}^{(\kappa\mid\kappa)}=\left(\mathbf{I}_{3L}-\mathbf{K}^{(\kappa)}\left(\boldsymbol{\rho}^{(\kappa)}\otimes\mathbf{I}_2\right)\tilde{\mathbf{G}}^{(\kappa\mid\kappa-1)}\right)\mathbf{P}^{(\kappa\mid\kappa-1)}$
if $\left\lvert\hat{\psi}_{\mathrm{UE},l}^{(\kappa)}-\bar{\psi}_{\mathrm{UE},l}^{(\kappa)}\right\rvert\geq\gamma$ **then**
$\hat{x}_l^{(\kappa\mid\kappa)}=x_l^{(\kappa-1)}+\nu_l^{(\kappa-1)}T_s\cos\varphi_l$
$\hat{y}_l^{(\kappa\mid\kappa)}=y_l^{(\kappa-1)}+\nu_l^{(\kappa-1)}T_s\sin\varphi_l$
$\hat{\nu}_l^{(\kappa\mid\kappa)}=\nu_{\ell-1}$
end if
end for

performance. Therefore, this paper introduces an angular deviation correction mechanism at the end of the EKF algorithm iterations to correct the state variables that exceed the threshold value, suppressing the cumulative error, and at the same time ensuring fairness among multiple vehicles without the communication quality of one vehicle being too poor. Define the deviation threshold γ. When the angular deviation exceeds the threshold γ, that is, $|\hat{\psi}_{\mathrm{UE},l}^{(\kappa)}-\bar{\psi}_{\mathrm{UE},l}^{(\kappa)}|\geq\gamma$, it is convenient to correct it based on the state information obtained through broadcasting at the previous moment, where $\hat{\psi}_{\mathrm{UE},l}^{(\kappa)}$ is the a posteriori estimate in the EKF algorithm, and $\bar{\psi}_{\mathrm{UE},l}^{(\kappa)}$ is the a priori estimate. These two angles can be derived according to Eq. (19). The calibration process is as follows:

$$\hat{x}_l^{(\kappa\mid\kappa)} = x_l^{(\kappa-1)}+\nu_l^{(\kappa-1)}T_s\cos\varphi_l \tag{86}$$

$$\hat{y}_l^{(\kappa\mid\kappa)} = y_l^{(\kappa-1)}+\nu_l^{(\kappa-1)}T_s\sin\varphi_l \tag{87}$$

$$\hat{\nu}_l^{(\kappa\mid\kappa)} = \nu_{\ell-1} \tag{88}$$

The multi-vehicle EKF beam tracking algorithm based on the angular deviation correction mechanism in this paper is shown in Table 1, where the computational complexity of the algorithm can be obtained as $O(N_n)$ based on the number of iterations. When initializing the parameters, it is assumed that there is $e_{\varepsilon}=\varepsilon\boldsymbol{\mu}^{(0)}$ feedback error in the initial state information of the vehicle obtained by the RSU. If the initial feedback error is modeled as A, the state vector is initialized as $\hat{\boldsymbol{\mu}}^{(0)}=\boldsymbol{\mu}^{(0)}+e_{\varepsilon}$, that is, the situation of beam tracking under non-ideal feedback signal conditions is considered, where $\varepsilon\sim N(0,\sigma_{\varepsilon}^2)$ is the feedback error parameter.

4. SIMULATION RESULTS AND ANALYSIS

In this section, the multi-vehicle beam tracking system with the introduction of ARIS assistance is simulated and analyzed. Comparison of beam tracking performance is evaluated by using root-mean-square error (RMSE) $\mathrm{M}_x=\sqrt{\frac{1}{T}\sum_{l=1}^{L}\sum_{\kappa=1}^{T}|x_l^{(\kappa)}-\hat{x}_l^{(\kappa)}|^2}$ and $\mathrm{M}_y=\sqrt{\frac{1}{T}\sum_{l=1}^{L}\sum_{\kappa=1}^{T}|y_l^{(\kappa)}-\hat{y}_l^{(\kappa)}|^2}$ for different scenarios. In this paper, the center frequency of the system is considered to be $f_c=28\,\mathrm{GHz}$, and the noise power magnitude is $\sigma^2=-101\,\mathrm{dBm}$. The default number of antennas at the receiver and transmitter is 16; the path loss index is $n=2$; the time slot period size is $T_s=10\,\mathrm{ms}$; and the RSU height is set to $h_{\mathrm{RSU}}=10\,\mathrm{m}$. The total number of vehicles, $L=3$, is assumed to have initial positions $(-30,10)$, $(-25,8)$, and $(-20,5)$, all with initial speeds $v_0=10\,\mathrm{m/s}$, all with deflection angles $\pi/2^7$, and traveling for a duration of 1 s. The height of ARIS is set to $h_{\mathrm{ARIS}}=15\,\mathrm{m}$, the array size to 4×4, and the coordinates to $(x_{\mathrm{ARIS}},y_{\mathrm{ARIS}})=(0,15)$. The error parameter is assumed to follow a Gaussian distribution with a standard deviation of $\sigma_{\omega}=10^{-1}$. The reference communication channel parameters are $\tilde{\beta}=1$, the beam merging vector weights $\tau=0.5$, and the deviation threshold $\gamma=0.001$. First consider the case of beam tracking under the condition of ideal feedback signal, that is, $\sigma_{\varepsilon}=0$. The detailed simulation parameters are shown in Table 2.

Figure 4 compares the beam tracking performance of multi-vehicle with respect to x-coordinate and y-coordinate at different launch powers, where the simulation mainly compares the joint beamforming scheme proposed in this paper, the random RIS reflective beamforming scheme, and the joint beamforming scheme that applies [24] to a single RIS scenario. In the random RIS reflection beamforming scheme, the phase shifts of all the RIS cells follow a uniform distribution of $[0,2\pi)$. As can be seen in Figure 4, the performance of all the schemes improves with the increase in transmitting power. This is because as the transmission power increases, the effective signal strength re-

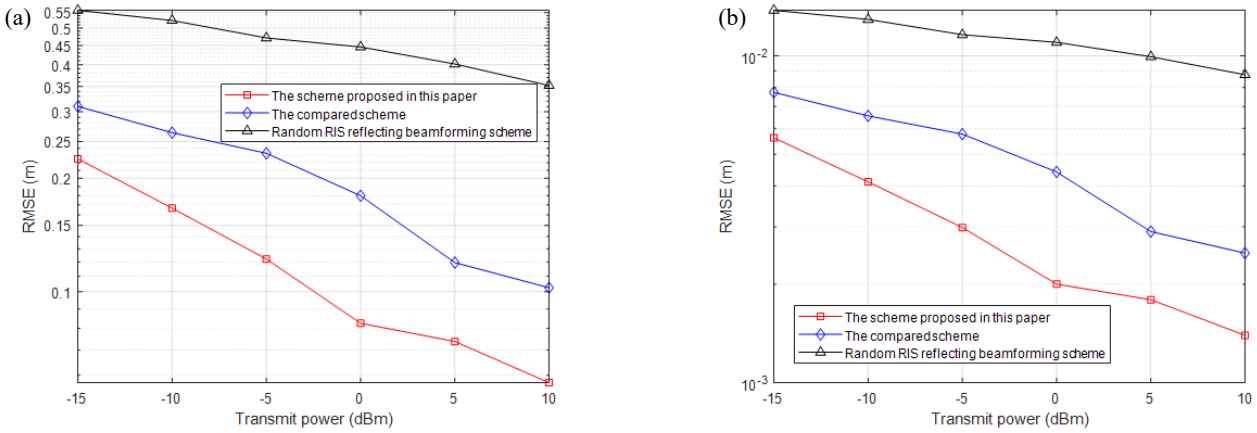

FIGURE 4. Comparison of multi-vehicle beam tracking performance with different beamforming schemes. (a) Tracking performance in x-coordinate. (b) Tracking performance in y-coordinate.

TABLE 2. System simulation parameters.

Simulation parameters	Retrieve value
Carrier frequency f_c	28 GHz (s)
Noise power σ^2	-101 dBm
Number of transmitter antennas N_{T}	16
Number of receiving end antennas N_{R}	16
Path loss index n	2
Time slot cycle T_s	10 ms
Total number of vehicles L	3
Vehicle initial position	$(-30, 10)$, $(-25, 8)$, $(-20, 5)$
Initial vehicle speed ν_0	10 m/s
Vehicle deflection angle φ	$\pi/2^7$
RSU height h_{RSU}	10 m
ARIS height h_{ARIS}	15 m
Number of ARIS array elements $N_{\mathrm{ARIS}} = N_{\mathrm{x}} \times N_{\mathrm{y}}$	4×4
ARIS coordinates $(x_{\mathrm{ARIS}}, y_{\mathrm{ARIS}})$	$(0, 15)$
Error parameter σ_ω	10^{-1}
Feedback error parameters σ_ε	0
Beam Merge Vector Weights τ	0.5
Deviation threshold γ	0.001
Power gain factor $\tilde{\beta}$	1

ceived by each vehicle also increases, that is, the SNR will also be improved. It means that there is less noise disturbance, and therefore there will be better beam tracking performance. Compared with the other two algorithms, the joint beamforming scheme proposed in this paper has better effect, a better ability to utilize the transmission power, and requires less transmission power when achieving the same beam tracking performance. The poor enhancement of the RIS stochastic phase-shift scheme is due to the lack of beamforming optimization of the RIS, and thus plays only a weak role in optimizing the sum rate of the multi-vehicle system, which also illustrates the importance of the design of the phase-shift for the RIS. Regarding the beam tracking performance in x-coordinate and y-coordinate, the tracking error decreases with the increase of transmit power in both cases, and the tracking error in y-coordinate is lower than that in x-coordinate. This is because in the established coordinate system, the main direction of travel of the vehicle coincides with the x-axis direction, and the movement on the y-axis is due to the deflection of the vehicle's motion being taken into account, but this deflection is at a smaller angle, which leads to a smaller tracking error in the y-coordinate than in the x-coordinate. For the sake of simulation simplicity and focusing on the core problem, only the x-coordinate, which has a larger tracking error and represents the main motion direction of the vehicle, is selected as the simulation object.

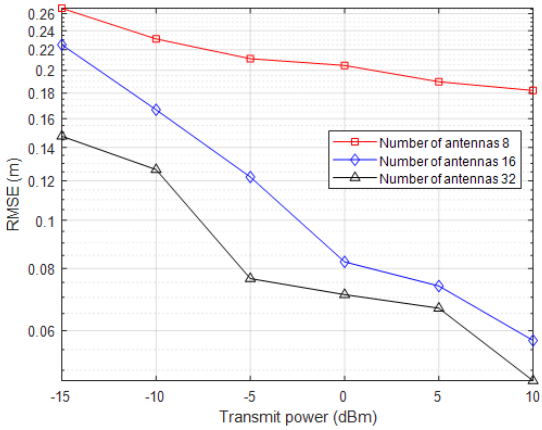

FIGURE 5. Comparison of multi-vehicle beam tracking performance with different numbers of transmitting antennas.

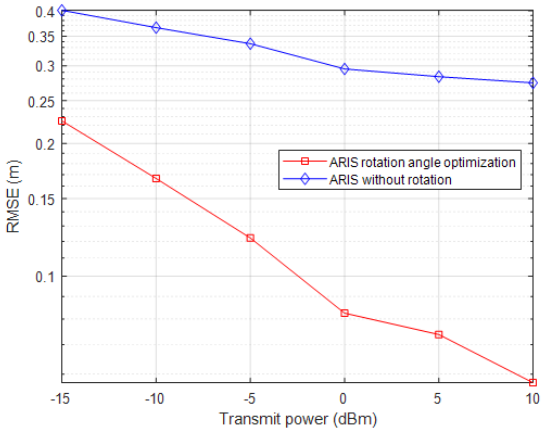

FIGURE 6. Effect of ARIS rotational characteristics on multi-vehicle beam tracking performance.

Figure 5 compares the effect of the number of transmitting antennas on the multi-vehicle beam tracking performance. From Figure 5, it can be seen that the tracking error is minimized when the number of antennas is 32, and the tracking error is maximized when the number of antennas is 8, i.e., the more the number of antennas is, the smaller the beam tracking error is. This is because as the number of antennas increases, the beam gain is higher, and beamforming enables the generation of narrower, more energy-focused beams, resulting in continuously improved signal quality and directivity. It means that the beam tracking performance of the system can be improved by increasing the number of transmit antennas at the base station for the same transmit power. From the array antenna principle, it can be seen that with the increase in the number of antennas, the beam will become narrower, although it can significantly improve the beam pointing accuracy, but when the vehicle is traveling at high speeds, this will increase the difficulty of beam alignment, which in turn reduces the performance of beam tracking. Therefore, the number of transmitting antennas needs to be set reasonably according to the actual scenario.

Figure 6 compares the effect of ARIS rotation angle optimization on multi-vehicle beam tracking performance. From Figure 6, it can be seen that the optimization of ARIS rotation angle plays an important role in improving the performance of beam tracking, which is because the reflected beam can be directed more accurately to the target vehicle by the rotation of the ARIS, and the beamforming gain can be improved. This shows that introducing the rotational property of ARIS makes RIS more directional and also influences the phase shift design of the RIS reflector unit, which provides an effective degree of freedom for beamforming optimization to adjust the beam angle in real time according to the position and speed information of the vehicle, and reduces the problem of beam misalignment due to the movement of the vehicle, so as to maintain a stable communication link.

Figure 7 compares the effect of different initial speeds on the tracking performance of the multi-vehicle beam. From Figure 7, it can be seen that the tracking error is maximum at a speed of 10 m/s and minimum at a speed of 30 m/s. It is known that

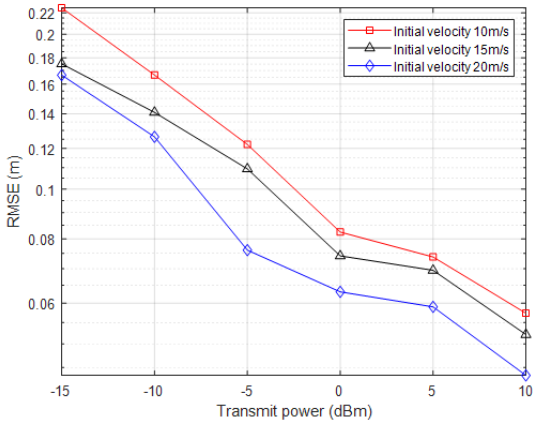

FIGURE 7. Comparison of multi-vehicle beam tracking performance with different initial speeds.

the faster the speed is, the greater the distance is traveled by the vehicle in a unit of time, and the tracking beam cannot be quickly switched to the optimal communication beam, which causes a certain tracking lag and makes the accuracy of beam alignment greatly reduced. In this paper, by introducing an angular deviation correction mechanism in the EKF algorithm, the faster the speed is, the larger the angular deviation is between the receiving and transmitting end beams, then the state information obtained at the previous moment will be frequently utilized to make corrections, thus making the system tracking error lower. In addition, from the initial moment, all the vehicles in the scene approach the RSU, and from Eq. (3), the shorter the distance of the path, the larger the average SNR of the antenna, then the tracking error is reduced. But that doesn't mean that the faster the speed, the better the tracking performance. The ability to improve the filtering accuracy by using this mechanism is limited. As can be seen from Eq. (61), this correction mechanism does not consider the influence of the error transfer vector. Therefore, as time increases, errors will continuously accumulate. Moreover, in the later stage of driving, the vehicle will continuously move away from the RSU, thereby resulting in a significant reduction in system performance.

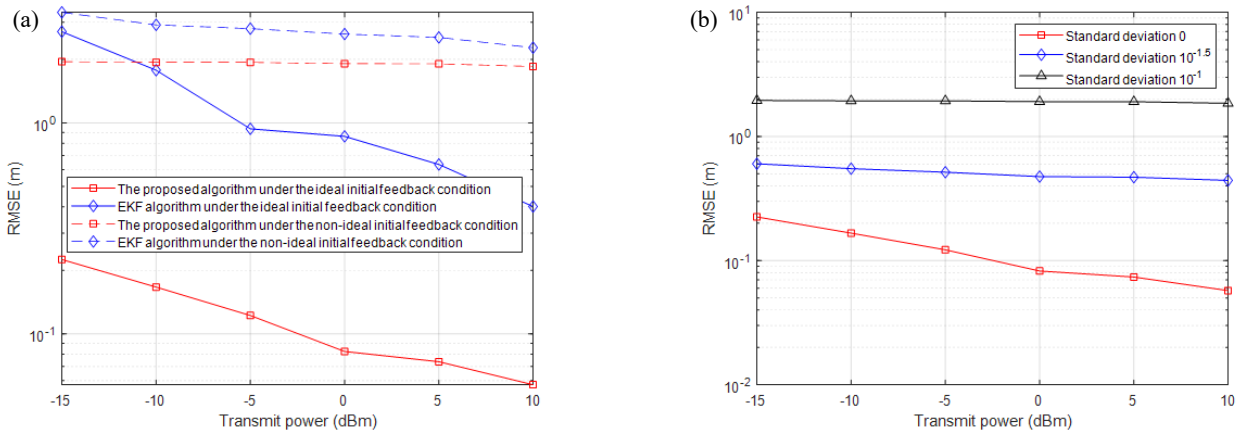

FIGURE 8. Comparison of multi-vehicle beam tracking performance of different algorithms. (a) Comparison of beam tracking algorithms under different initial feedback conditions. (b) Effect of initial feedback error parameters on beam tracking performance.

Figure 8 compares the multi-vehicle beam tracking performance of the proposed beam tracking algorithm with the conventional EKF algorithm. Meanwhile, in order to further verify the robustness of the proposed beam tracking algorithm, the simulation performances of the two algorithms under ideal and non-ideal initial feedback conditions are compared, where $\sigma_\varepsilon = 10^{-1.5}$. Moreover, the multi-vehicle beam tracking performance is simulated using the proposed beam tracking algorithm under different initial feedback error parameters, where the standard deviation of the feedback error parameter is set to $\sigma_\varepsilon = \{0, 10^{-1.5}, 10^{-1}\}$. As can be seen from Figure 8(a), under ideal initial feedback conditions, compared with the traditional EKF algorithm, this paper further improves the performance of beam tracking by introducing the angular deviation correction mechanism, which effectively suppresses the accumulation of estimation error over time. Under non-ideal initial feedback conditions, the tracking error of the proposed algorithm in this paper is still smaller than that of the traditional EKF algorithm. In addition, it can be seen from Figure 8(b) that the smaller the initial feedback error is, the smaller the influence on the initial state information of the vehicle is, and thus the beam tracking performance obtained is good. In summary, the proposed beam tracking algorithm works better than the traditional EKF algorithm, as well as verifies that the proposed beam tracking algorithm has a more robust beam tracking capability under non-ideal conditions.

5. CONCLUSION

In this paper, ARIS-assisted multi-vehicle beam tracking based on millimeter-wave MIMO networks in V2I communication scenarios is investigated by taking advantage of UAV and RIS technologies. The beam tracking model for ARIS-assisted multi-vehicle communication scenarios is derived by jointly designing the beam merging matrix at the user side, the reflective beamforming matrix at the RIS side, and the rotation angle of ARIS to maximize the system and rate, and an EKF algorithm based on the angular deviation correction mechanism is proposed to realize beam tracking for multi-vehicles. Simulation results show that based on the above joint design scheme and the proposed EKF algorithm, the error of multi-vehicle beam tracking can be significantly reduced. However, in real communication systems, it is difficult to represent the RIS-assisted wireless communication system model by an accurate mathematical model, and the corresponding computational overhead is high due to the mobility of the users, the complexity of the communication environment, and the uncertainty of the interference. So subsequently, the design of beamforming can be considered using artificial intelligence algorithms to overcome the limitations of traditional optimization algorithms.

ACKNOWLEDGEMENT

This work was supported by the Natural Science Foundation of Fujian Province (Grant No. 2022J011276, and No. 2023I0044), Undergraduate Education and Teaching Research Project of Fujian Province (Grant No. FBJY20240120), High-level Talent Project of Xiamen University of Technology (Grant No. YKJ22030R, and No. YKJ23034R), and Postgraduate Science and Technology Innovation Project of Xiamen University of Technology (Grant No. YKJCX2024143).

REFERENCES

[1] Meng, X., F. Liu, C. Masouros, W. Yuan, Q. Zhang, and Z. Feng, "Vehicular connectivity on complex trajectories: Roadway-geometry aware ISAC beam-tracking," *IEEE Transactions on Wireless Communications*, Vol. 22, No. 11, 7408–7423, 2023.

[2] Yu, X., L. Tu, Q. Yang, M. Yu, Z. Xiao, and Y. Zhu, "Hybrid beamforming in mmWave massive MIMO for IoV with dual-functional radar communication," *IEEE Transactions on Vehicular Technology*, Vol. 72, No. 7, 9017–9030, 2023.

[3] Saqib, N. U., S. Hou, S. H. Chae, and S.-W. Jeon, "Reconfigurable intelligent surface aided hybrid beamforming: Optimal placement and beamforming design," *IEEE Transactions on Wireless Communications*, Vol. 23, No. 9, 12 003–12 019, 2024.

[4] Sun, Y., C.-W. Feng, X.-L. Wang, J.-N. Yuan, and L. Zhang, "Beam tracking based on a new state model for mmWave V2I communication on 3D roads," *Journal of Computers*, Vol. 35, No. 1, 33–50, 2024.

[5] Wu, Q., S. Zhang, B. Zheng, C. You, and R. Zhang, "Intelligent reflecting surface-aided wireless communications: A tutorial," *IEEE Transactions on Communications*, Vol. 69, No. 5, 3313–3351, 2021.

[6] Chen, W., X. Lin, J. Lee, A. Toskala, S. Sun, C. F. Chiasserini, and L. Liu, "5G-advanced toward 6G: Past, present, and future," *IEEE Journal on Selected Areas in Communications*, Vol. 41, No. 6, 1592–1619, 2023.

[7] Tian, Y., B. Xiao, X. Wang, Y. H. Kho, C. Zhu, W. Li, Q. Li, and X. Hu, "Opportunistic RIS-assisted rate splitting transmission in coordinated multiple points networks," *Computer Communications*, Vol. 202, 23–32, 2023.

[8] Xiao, B., Y. Tian, W. Li, Y. H. Kho, X. Wang, C. Zhu, and H. Liu, "Performance analysis of adaptive RIS-assisted clustering strategies in downlink communication systems," *IEEE Internet of Things Journal*, Vol. 10, No. 5, 4520–4530, 2023.

[9] Teng, B., X. Yuan, R. Wang, and S. Jin, "Bayesian user localization and tracking for reconfigurable intelligent surface aided MIMO systems," *IEEE Journal of Selected Topics in Signal Processing*, Vol. 16, No. 5, 1040–1054, 2022.

[10] Tian, Y., B. Xiao, X. Wang, Y. H. Kho, and C. Tian, "Performance analysis of opportunistic NOMA strategy in uplink coordinated multi-points systems," *Computer Communications*, Vol. 177, 207–212, 2021.

[11] Pan, C., G. Zhou, K. Zhi, S. Hong, T. Wu, Y. Pan, H. Ren, M. D. Renzo, A. L. Swindlehurst, R. Zhang, and A. Y. Zhang, "An overview of signal processing techniques for RIS/IRS-aided wireless systems," *IEEE Journal of Selected Topics in Signal Processing*, Vol. 16, No. 5, 883–917, 2022.

[12] Yao, J., W. Xu, Y. Huang, H. H. Xiao, and Z. H. Lu, "Techniques for reconfigurable intelligent surface-aided 6G communication network: An overview," *Journal of Signal Processing*, Vol. 38, No. 8, 1555–1567, 2022.

[13] You, C., Z. Kang, Y. Zeng, and R. Zhang, "Enabling smart reflection in integrated air-ground wireless network: IRS meets UAV," *IEEE Wireless Communications*, Vol. 28, No. 6, 138–144, 2021.

[14] Lu, H., Y. Zeng, S. Jin, and R. Zhang, "Aerial intelligent reflecting surface: Joint placement and passive beamforming design with 3D beam flattening," *IEEE Transactions on Wireless Communications*, Vol. 20, No. 7, 4128–4143, 2021.

[15] Yang, L. and W. Zhang, "Beam tracking and optimization for UAV communications," *IEEE Transactions on Wireless Communications*, Vol. 18, No. 11, 5367–5379, 2019.

[16] Wang, X., H. Zhang, H. Yang, Y. Tian, C. Zhu, and A. Nallanathan, "A non-orthogonal cross-tier joint transmission design for clustered ABS-assisted networks," *IEEE Transactions on Wireless Communications*, Vol. 23, No. 4, 3361–3376, 2024.

[17] Wang, X., H. Zhang, K. J. Kim, Y. Tian, and A. Nallanathan, "Performance analysis of cooperative aerial base station-assisted networks with non-orthogonal multiple access," *IEEE Transactions on Wireless Communications*, Vol. 18, No. 12, 5983–5999, 2019.

[18] Cui, Y., Z. Ying, P. He, Y. Zheng, D. Wu, R. Wang, and L. Chen, "Ultra-reliable low-latency communication multi-unmanned aerial vehicle network assisted by intelligent reflecting surface in air," *Journal of Southwest Jiaotong University*, Vol. 59, No. 4, 907–916, 2024.

[19] Muntaha, S. T., N. U. Hassan, I. H. Naqvi, and C. Yuen, "Aerial reconfigurable intelligent surface: Rotate or displace?" in *2022 IEEE 33rd Annual International Symposium on Personal, Indoor and Mobile Radio Communications (PIMRC)*, 566–571, Kyoto, Japan, 2022.

[20] Xie, T., Q. Tao, X. Gan, and C. Zhong, "UKF-based channel tracking method for IRS-aided mmwave MISO Systems," *IEEE Communications Letters*, Vol. 27, No. 6, 1599–1603, 2023.

[21] Yu, D., G. Zheng, A. Shojaeifard, S. Lambotharan, and Y. Liu, "Kalman filter based channel tracking for RIS-assisted multi-user networks," *IEEE Transactions on Wireless Communications*, Vol. 23, No. 4, 3856–3869, 2024.

[22] Ge, Z., D. Yue, G. Li, S. Wei, and Y. Su, "Beamforming design of millimeter wave MIMO system assisted by intelligent reflecting surface," *Telecommunication Engineering*, Vol. 63, No. 01, 7–13, 2023.

[23] Van Chien, T., B. T. Duc, H. V. D. Luong, H. T. T. Binh, H. Q. Ngo, and S. Chatzinotas, "Active and passive beamforming designs for SER minimization in RIS-assisted MIMO systems," *IEEE Transactions on Wireless Communications*, Vol. 23, No. 12, 18 838–18 854, 2024.

[24] Shabir, M. W., T. N. Nguyen, J. Mirza, B. Ali, and M. A. Javed, "Transmit and reflect beamforming for max-min SINR in IRS-aided MIMO vehicular networks," *IEEE Transactions on Intelligent Transportation Systems*, Vol. 24, No. 1, 1099–1105, 2023.

[25] Adam, A. B. M., M. A. Ouamri, X. Wan, M. S. A. Muthanna, R. Alkanhel, A. Muthanna, and X. Li, "Secure communication in UAV-RIS-empowered multiuser networks: Joint beamforming, phase shift, and UAV trajectory optimization," *IEEE Systems Journal*, Vol. 18, No. 2, 1009–1019, 2024.

[26] Yang, Y., H. Hu, F. Zhou, L. Yang, and R. Q. Hu, "Robust beamforming and phase shift optimization for RIS-assisted UAV multiuser MISO communication networks," *IEEE Transactions on Vehicular Technology*, Vol. 73, No. 10, 15 687–15 692, 2024.

[27] Zhang, J., Z. Zheng, Z. Fei, Z. Chang, and Z. Han, "RIS-assisted multi-user localization in UAV-enabled mmWave wireless networks," *IEEE Transactions on Vehicular Technology*, Vol. 74, No. 3, 5069–5084, 2025.

[28] Nguyen, M.-H. T., E. Garcia-Palacios, T. Do-Duy, O. A. Dobre, and T. Q. Duong, "UAV-aided aerial reconfigurable intelligent surface communications with massive MIMO system," *IEEE Transactions on Cognitive Communications and Networking*, Vol. 8, No. 4, 1828–1838, 2022.

[29] Song, J., S.-H. Hyun, J.-H. Lee, J. Choi, and S.-C. Kim, "Joint vehicle tracking and RSU selection for V2I communications with extended Kalman filter," *IEEE Transactions on Vehicular Technology*, Vol. 71, No. 5, 5609–5614, 2022.

[30] Hyun, S.-H., J. Song, K. Kim, J.-H. Lee, and S.-C. Kim, "Adaptive beam design for V2I communications using vehicle tracking with extended kalman filter," *IEEE Transactions on Vehicular Technology*, Vol. 71, No. 1, 489–502, 2022.

[31] Song, J., J.-H. Lee, and S. Noh, "Position-based adaptive beamforming and roadside unit sectorization for V2I communications," *IEEE Transactions on Vehicular Technology*, Vol. 73, No. 2, 2960–2965, 2024.

[32] El Ayach, O., S. Rajagopal, S. Abu-Surra, Z. Pi, and R. W. Heath, "Spatially sparse precoding in millimeter wave MIMO systems," *IEEE Transactions on Wireless Communications*, Vol. 13, No. 3, 1499–1513, 2014.

[33] Liu, F., W. Yuan, C. Masouros, and J. Yuan, "Radar-assisted predictive beamforming for vehicular links: Communication served by sensing," *IEEE Transactions on Wireless Communications*, Vol. 19, No. 11, 7704–7719, 2020.

[34] Ribeiro, Y. S., A. L. F. de Almeida, Fazal-E-Asim, B. Makki, and G. Fodor, "Low-complexity joint active and passive beamforming design for IRS-assisted MIMO," *IEEE Wireless Communications Letters*, Vol. 13, No. 3, 607–611, 2024.

[35] Chen, X., Y. Huang, J. Shi, and R. Rui, "Joint beamforming for intelligent reflecting surface-aided multi-user massive MIMO system," *Telecommunication Engineering*, Vol. 63, No. 09, 1285–1290, 2023.

[36] Zappone, A., M. D. Renzo, F. Shams, X. Qian, and M. Debbah, "Overhead-aware design of reconfigurable intelligent surfaces in smart radio environments," *IEEE Transactions on Wireless Communications*, Vol. 20, No. 1, 126–141, 2021.

[37] Shaham, S., M. Ding, M. Kokshoorn, Z. Lin, S. Dang, and R. Abbas, "Fast channel estimation and beam tracking for millimeter wave vehicular communications," *IEEE Access*, Vol. 7, 141 104–141 118, 2019.